Atmospheric
Chemistry
and Physics

Sensitivity analysis of an aerosol-aware microphysics scheme in Weather Research and Forecasting (WRF) during case studies of fog in Namibia

Michael John Weston[1], **Stuart John Piketh**[2], **Frédéric Burnet**[3], **Stephen Broccardo**[2,a], **Cyrielle Denjean**[3], **Thierry Bourrianne**[3], and **Paola Formenti**[4]

[1]Research and Development Division, Khalifa University, Abu Dhabi, UAE
[2]School of Geo- and Spatial Science, North-West University, Potchefstroom, South Africa
[3]CNRM, Université de Toulouse, Météo-France, CNRS, Toulouse, France
[4]Université Paris Cité and Univ Paris Est Creteil, CNRS, LISA, 75013 Paris, France
[a]now at: Bay Area Environmental Research Institute/NASA Ames Research Center, Moffett Field, CA, USA

Correspondence: Stuart John Piketh (stuart.piketh@nwu.ac.za)

Abstract. Aerosol-aware microphysics parameterisation schemes are increasingly being introduced into numerical weather prediction models, allowing for regional and case-specific parameterisation of cloud condensation nuclei (CCN) and cloud droplet interactions. In this paper, the Thompson aerosol-aware microphysics scheme, within the Weather Research and Forecasting (WRF) model, is used for two fog cases during September 2017 over Namibia. Measurements of CCN and fog microphysics were undertaken during the AErosols, RadiatiOn and CLOuds in southern Africa (AEROCLO-sA) field campaign at Henties Bay on the coast of Namibia during September 2017. A key concept of the microphysics scheme is the conversion of water-friendly aerosols to cloud droplets (hereafter referred to as CCN activation), which could be estimated from the observations. A fog monitor 100 (FM-100) provided cloud droplet size distribution, number concentration (N_t), liquid water content (LWC), and mean volumetric diameter (MVD). These measurements are used to evaluate and parameterise WRF model simulations of N_t, LWC, and MVD. A sensitivity analysis was conducted through variations to the initial CCN concentration, CCN radius, and the minimum updraft speed, which are important factors that influence droplet activation in the microphysics scheme of the model. The first model scenario made use of the default settings with a constant initial CCN number concentration of $300 \, \text{cm}^{-3}$ and underestimated the cloud droplet number concentration, while the LWC was in good agreement with the observations. This resulted in droplet size being larger than the observations. Another scenario used modelled data as CCN initial conditions, which were an order of magnitude higher than other scenarios. However, these provided the most realistic values of N_t, LWC, MVD, and droplet size distribution. From this, it was concluded that CCN activation of around 10 % in the simulations is too low, while the observed appears to be higher reaching between 20 % and 80 %, with a mean (median) of 0.55 (0.56) during fog events. To achieve this level of activation in the model, the minimum updraft speed for CCN activation was increased from 0.01 to $0.1 \, \text{m s}^{-1}$. This scenario provided N_t, LWC, MVD, and droplet size distribution in the range of the observations, with the added benefit of a realistic initial CCN concentration. These results demonstrate the benefits of a dynamic aerosol-aware scheme when parameterised with observations.

1 Introduction

The central Namib desert is situated along a narrow coastal area about 100 km wide on the Namibian coast. It is adjacent to the cold Benguela Current in the South Atlantic Ocean and consequently experiences fog when the moist air from above the ocean is advected over the desert surface. As a vital source of fresh water in this arid ecosystem, fog has been a topic of study for decades (Cermak, 2012; Lancaster et al., 1984; Olivier, 1995; Seely and Henschel, 1998; Seely and Hamilton, 1976) and has recently motivated long-term distributed observations (the Fognet network, which is predominantly meteorological and radiation measurements; Muche et al., 2018) and intensive dedicated field campaigns (Spirig et al., 2019) that have shed new light on the spatial and temporal characteristics and dynamics of fog in the region (e.g. Andersen et al., 2019). Fog occurs predominantly at night and in early morning hours and is most frequent closer to the coast, reaching about 120 da year and decreasing to 40 (5) fog days at sites 40 (100) km inland (Olivier, 1995; Spirig et al., 2019; Andersen and Cermak, 2018; Cermak, 2012). Fog is most frequent in winter (May–August) at coastal sites and in summer (September–December) at inland sites (Andersen et al., 2019; Lancaster et al., 1984; Spirig et al., 2019; Olivier, 1995; Nagel, 1962). The fog is predominantly advective and high in elevation, corresponding to low stratus clouds that intersect with the land (Andersen et al., 2019, 2020). This is possible in the central Namib as the elevation gradually increases from the coast to 1000 m above sea level (m a.s.l.) at the escarpment about 100 km away to the east. In summer months, the stratus layer occurs at around 500 m a.s.l. (Andersen et al., 2019) and allows the fog to penetrate further inland. In winter, the stratus layer is lower, which limits fog to the coastal area.

Fog formation and lifetime is dependent on the atmospheric thermodynamic (radiation, turbulence, and mixing) and surface conditions (albedo, soil characteristics, roughness length, and moisture content). Therefore, the simulation of fog first requires that state atmospheric variables related to temperature and moisture are simulated adequately by models, which implies representing the coupling of land–atmosphere interactions and good parameterisation schemes of the planetary boundary layer (PBL; Bergot and Lestringant, 2019; Boutle et al., 2018; Juliano et al., 2019; Maronga and Bosveld, 2017; Steeneveld and De Bode, 2018).

Additionally, forecast of fog requires improved parameterisation of its microphysical properties (e.g. Bott, 1991; Gultepe and Milbrandt, 2007; Tardif, 2007). Several studies have demonstrated the importance of the cloud condensation nuclei (CCN) and cloud droplet relationship in simulating the fog life cycle (e.g. Boutle et al., 2018; Maalick et al., 2016; Stolaki et al., 2015). The formation of fog depends on the capabilities of the pre-existing aerosols to act as CCN, thereby providing a substrate for water vapour to condense and grow

to form a fog droplet. The properties of the CCN aerosols play a role in shaping the microphysics of the fog droplets (Gultepe and Milbrandt, 2007; Haeffelin et al., 2013). The size distribution of the droplets has an important effect of the radiation balance (Boutle et al., 2018; Egli et al., 2015; Mazoyer et al., 2019; Poku et al., 2019). Mazoyer et al. (2019) showed a widening of the droplet size distribution (DSD) towards the fog top as droplets grew by collision and coalescence. Egli et al (2015) showed that liquid water content (LWC) varies through the fog layer, usually with a maximum near the centre of the fog layer. In this case, the increase in LWC was due to an increase in number concentration and not the conversion of small droplets to larger droplets. These complex microphysical processes within the fog layer are increasingly being introduced into model simulations (Thompson and Eidhammer, 2014; Wilkinson et al., 2013).

Aerosol-aware microphysics schemes, with the main function of representing grid-scale clouds in a simulation (Thompson and Eidhammer, 2014; Wilkinson et al., 2013), are now being used to represent fog in the lowest model level and are showing encouraging results. Boutle et al. (2018) and Poku et al. (2019) demonstrated improved fog simulations of cloud droplet number and sedimentation based on model sensitivity to CCN concentrations in an aerosol-aware scheme. Mazoyer et al. (2019) demonstrated that improving the supersaturation and activation of CCN ameliorated the forecast results of droplet concentration. As these schemes advance, more detailed information on CCN size distribution, chemistry, and activation can be provided as input to models, in particular in numerical weather prediction (NWP) models, when they are often represented by implementing a lookup table of CCN activation (see Ghan et al., 2011; Saleeby and Cotton, 2004).

Microphysics schemes in mesoscale models are designed with cloud formation in mind and not necessarily fog formation. Droplet activation is based on a parcel that is lifted and cooled adiabatically to reach saturation and is therefore most sensitive to the updraft speed. However, fog often occurs under stable conditions where updrafts are low in speed or even negative. Thus, droplet activation is dependent on other processes like non-adiabatic cooling. This point is highlighted by Boutle et al. (2018), who observe a cooling rate prior to fog formation of $1\,\mathrm{K\,h^{-1}}$, which is equivalent to an updraft speed of $0.04\,\mathrm{m\,s^{-1}}$, assuming a wet adiabatic lapse rate of $6.5\,\mathrm{K\,km^{-1}}$. In their case, the minimum updraft speed in the microphysics scheme was $0.1\,\mathrm{m\,s^{-1}}$ and, thus, would overestimate fog drop activation. To address this issue, Poku et al. (2021) expanded an existing microphysics scheme to allow for non-adiabatic cooling, which allowed for more realistic cloud droplet number concentration in the simulation.

In this paper, we assess an aerosol-aware microphysics scheme that uses a minimum updraft speed of $0.01\,\mathrm{m\,s^{-1}}$, which equates to a cooling rate of $0.23\,\mathrm{K\,h^{-1}}$. This minimum updraft speed should solve some of the over-activation issues highlighted by Boutle et al. (2018) and Poku et al. (2019).

The main aim is to see how this scheme performs before applying major changes in the code to account for non-adiabatic cooling rates or similar. Furthermore, our study site is located in the tropics, which we see as a benefit to the community at large, as most fog modelling studies are focused on mid- to high-latitude sites.

In this paper, we present an assessment of the capabilities of the Weather Research and Forecasting (WRF) model to predict two fog events observed in September 2017 along the coast of Namibia. WRF has been used to simulate fog previously using rule-based methods (Román-Cascón et al., 2016; Weston et al., 2021); however, we will focus on the aerosol-aware microphysics scheme capabilities in the model. The area is interesting for studying fog formation as the contribution of anthropogenic sources to the background aerosol concentration is limited, meaning that pollution is minimal. Namibia has a population density of 3 people km^{-2} (Statista, 2020), and previous research has shown that the influence of anthropogenic activities is minor (Formenti et al., 2019; Klopper et al., 2020).

Fog is diagnosed from the model using the LWC from an aerosol-aware microphysics parameterisation scheme. This work takes advantage of the measurements of surface level fog microphysics that were performed at a ground-based site on the coast of Namibia as part of the AErosols, RadiatiOn and CLOuds in southern Africa (AEROCLO-sA) campaign (Formenti et al., 2019).

The work is structured as follows. In Sect. 2, a description of the study sites, data sets, and model configuration is presented. Section 3 includes the model results and discussion. A summary of the main findings is given Sect. 4.

2 Methodology

2.1 Study area

The central Namib is a coastal desert on the coast of Namibia. It lies between the Atlantic Ocean to the west and the escarpment over 1000 m in elevation about 100 km to the east. The mean annual rainfall is highest at the escarpment (100 mm) and decreases towards the coast (< 50 mm; Lancaster et al., 1984; Spirig et al., 2019). The land cover type undergoes a stark transition at the ephemeral Kuiseb River, with the rocky gravel plains to the north and large sand dunes to the south. Surface airflow along the coast is dominated by an onshore wind, predominantly from the southwest (Lindesay and Tyson, 1990). This flow can be amplified by the synoptic scale circulation of the South Atlantic high pressure system. However, the onshore flow does not penetrate far inland where the surface airflow is controlled by the mountain–plain wind. The easterly wind is much drier and limits moisture transport inland. As a result, fog forms in a narrow band along the coastline.

2.2 Model configuration

The Weather Research and Forecast model (WRF v3.9.1; Skamarock et al, 2008) was used to forecast next-day fog. In total, three nested domains with horizontal grid resolutions of 27, 9, and 3 km were defined, and the model was run with one-way nesting (Fig. 1). The parent domain, domain 1, was sufficiently large to allow the movement of low pressure cells in the easterlies and westerlies to pass through and provide boundary conditions to the nested domains. Domain 2 extended 4266 km from east to west and 2296 km from north to south. Domain 3 was constructed with the study site approximately in the centre and extended 1386 km from east to west and 720 km north to south. A total of 50 vertical levels were used, with extra vertical levels added near the surface to allow for 11 model levels below 500 m above ground level (a.g.l.). This was decided after initial simulations demonstrated that the default vertical resolution was too coarse near the fog top. The mean height of the lowest five levels was 34, 71, 109, 146, and 184 m a.g.l. Boutle et al. (2022) evaluated results from large eddy simulation (LES) and single column models (SCMs) for a radiation fog case in the United Kingdom and recommend having a first vertical level of less than 10 m and six or more levels below 150 m. An increase in the vertical resolution is expected to better simulate strong moisture and temperature gradients in the lower troposphere (e.g. Branch et al., 2021). However, Ajjaji et al. (2008) reported that an increase in the vertical resolution can have the opposite effect and inhibit cloud formation for fog events over the United Arab Emirates, an arid region similar to Namibia, during a WRF real-case (i.e. not SCM) simulation. Furthermore, our set-up is in line with the vertical profiles reported in the literature which show that the moisture is trapped below 500 m (e.g. Andersen et al., 2019; Formenti et al., 2019; Spirig et al., 2019). The model was initialised at 06:00 UTC (08:00 local time, LT) with Global Forecast System (GFS v14) data at 0.25° resolution and updated every 6 h (NCEP, 2015).

Sea surface temperature (SST) from the GFS was allowed to follow a diurnal cycle in WRF using the method described by Zeng and Beljaars (2005). This means that 6 h values from the GFS are interpolated to provide hourly updated values in WRF. The Noah land surface model was used with land cover classes from the United States Geological Survey (USGS; Loveland et al., 2000; Sertel et al., 2010). The default soil texture in WRF is from the State Soil Geographic (STATSGO)/Food and Agriculture Organization (FAO) soil database (Dy and Fung, 2016; Sanchez et al., 2009).

Shortwave and longwave radiation was controlled by the rapid radiation model for general circulation model applications (RRTMG; Iacono et al., 2008). The revised MM5 (Fifth-Generation Mesoscale Model) scheme was used for the surface layer and the Mellor–Yamada–Nakanishi–Niino level 2.5 (MYNN2.5) scheme for the planetary boundary layer (PBL) physics parameterisation (Nakanishi and Niino,
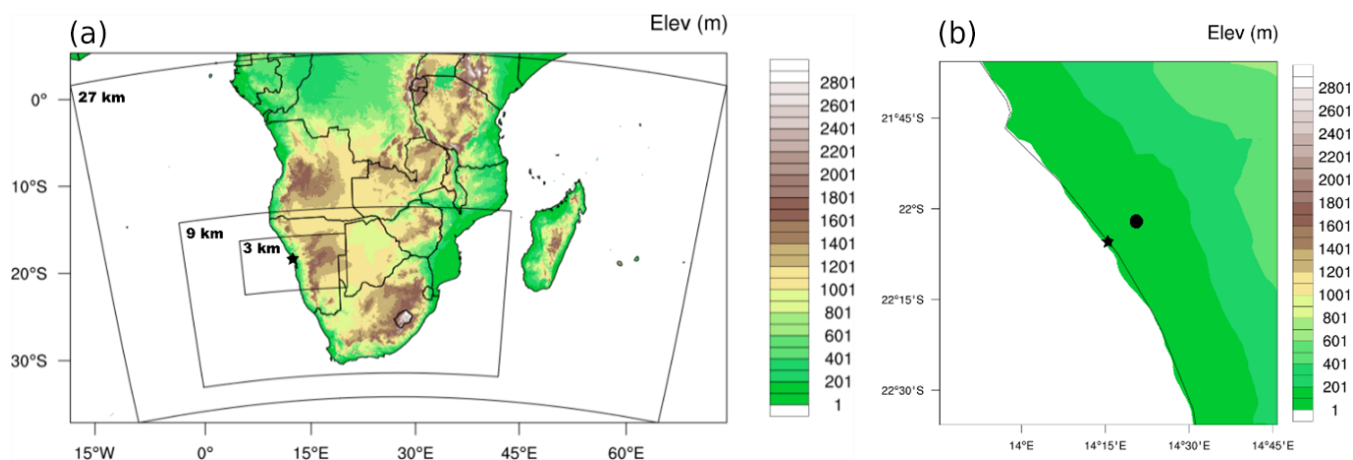
Figure 1. (a) WRF model domains and **(b)** insert showing the Henties Bay site (star) and inland point (circle) from the model which is used during the evaluation of the simulations.

2006). The Kain–Fritsch cumulus physics was activated in domain 1 but deactivated in domain 2 and 3 (Kain, 2004). This allows for subgrid-scale precipitation in the coarse resolution parent domain, allowing for realistic water balance when applying one-way nesting.

2.2.1 Fog microphysics

The grid-scale cloud microphysics bulk scheme by Thompson and Eidhammer (2014) assumes a gamma distribution of cloud DSD for droplet diameters, D, comprised between 1 to 100 μm. It is worth noting that the scheme accounts for the conversion of cloud droplets to rain droplets, which are treated separately, and the rain DSD spans a wider range in diameter. The number concentration per cloud droplet diameter, $N(D)$ is calculated as follows:

$$N(D) = \frac{N_t}{\Gamma(\mu+1)}\lambda^{\mu+1}D^{\mu}e^{-\lambda D}, \tag{1}$$

where N_t is the total cloud droplet number concentration (cm^{-3}), Γ is the gamma function, μ is the shape parameter, and λ is the slope. It is a double moment scheme, meaning that cloud droplet mass and number concentration (N_t) is calculated from the DSD. The shape and slope parameters can be derived from N_t and liquid water content (LWC) as follows:

$$\mu = \min\left(\frac{1000}{N_t} + 2, 15\right), \tag{2}$$

where N_t is in cubic centimetres (cm^{-3}).

$$\lambda = \left[\frac{\pi}{6}\rho_w \frac{\Gamma(4+\mu)}{\Gamma(1+\mu)}\left(\frac{N_t}{\text{LWC}}\right)\right]^{\frac{1}{3}}, \tag{3}$$

where $\rho_w = 1000$ kg m^{-3} is water density, and LWC is in kilograms per cubic centimetre (kg cm^{-3}).

The median volume diameter (MVD) is calculated as follows:

$$\text{MVD} = \frac{3.672 + \mu}{\lambda}. \tag{4}$$

Fog was diagnosed when liquid water content was present in the lowest model level. This is a reasonable assumption for simulations with a suitably high resolution (i.e. observed fog feature is larger than model grid cell) and a sophisticated microphysics scheme (Zhou et al., 2012).

2.2.2 Configuration of the aerosol-aware sensitivity study

The Thompson aerosol-aware microphysics scheme (Thompson and Eidhammer, 2014; hereafter T14) was activated in all three domains to represent grid-scale cloud microphysics. This novel scheme accounts for the initial number concentration, mean radius, and hygroscopicity (kappa) of CCN and CCN activation to cloud (and other hydrometeor) droplets, which ultimately determine the maximum number of cloud droplets. Although the default settings for these variables are based on observations and the literature, users can refine the values based on their study area. For example, the initial CCN number concentration is set to 300 cm^{-3} at the lowest model level. This may not be appropriate for a particular study region or event and can be adjusted accordingly. Furthermore, the option exists to replace initial CCN with user-generated 3-D data fields of CCN as input. An example is provided with the model based on a 7-year climatology of aerosols produced by the NASA GEOS (Goddard Earth Observing System)-4 model (Colarco et al., 2010). A key approach of this scheme is the conversion of hygroscopic CCN, sometimes referred to as water-friendly aerosols, to cloud droplets. This is what is referred to as CCN activation in this document, which can

be thought of as the ratio of cloud droplets to hygroscopic CCN. CCN activation is based on parcel method simulations by Eidhammer et al. (2009). These simulations were used to create a look-up table (available within WRF) that varies the CCN activation to cloud droplets as a function of CCN number concentration, updraft speed, ambient temperature, CCN mean radius diameter, and kappa (hygroscopicity) values (Fig. 2). It is important to keep in mind that CCN activation in the scheme assigns a minimum updraft speed of $1\,\mathrm{cm\,s^{-1}}$ when air is saturated. This allows for droplet activation under saturated conditions via the look-up table, even when the simulated updraft is negative. An additional novelty of this scheme is that it allows feedback of CCN and cloud droplets to the radiation schemes in shortwave and longwave, which was activated in the model simulations.

Model scenarios were based on configuration of the microphysics, where the default CCN radius is $0.04\,\mu\mathrm{m}$ and the kappa is 0.4 (Fig. 3). Scenario 1 used the default initial CCN values of $300\,\mathrm{cm^{-3}}$ near the surface and $50\,\mathrm{cm^{-3}}$ in the free troposphere (hereafter CCN_300). The scheme applies a vertical profile to CCN concentration, allowing concentrations to decrease exponentially from the surface to the free troposphere (WRF Users Page, 2020; Fonseca et al., 2021). In summary, the scheme assigns the highest CCN concentration near the surface and follows an exponential decrease through the boundary layer to the minimum bound ($50\,\mathrm{cm^{-3}}$ in our case), which is then assigned to the lower free troposphere. The depth of the boundary layer is made to vary for different terrain heights, ranging to about 1000 m at sea level to less than 100 m where terrain is greater than 2500 m. The thinner boundary layer at increased terrain height would have a steeper drop-off in CCN concentration with height and subsequent dilution during daytime mixing. In CCN_300, the initial CCN concentration over land and ocean is the same. Thompson and Eidhammer (2014) proposed a different initial CCN concentration for land ($300\,\mathrm{cm^{-3}}$) and ocean ($100\,\mathrm{cm^{-3}}$) based on observations, as ocean air is generally cleaner and contains fewer CCN than continental air (Seinfeld and Pandis, 2016). We implemented this proposal for scenario 2 (hereafter CCN_300_landsea). The same treatment is applied to the vertical profile of CCN concentration as CCN_300. Scenario 3 is the default model setting using the 3-D climatology CCN modified from Colarco et al. (2010; hereafter CCN_C10). As this is a 3-D data set, no idealised vertical profile is applied at initialisation. Simulations were run from 7 to 10 September 2017 to coincide with the best data from the fog monitor 100 (FM-100) instrument. Recall that simulations are initialised at 06:00 UTC and were run for 48 h. The first 6 h are discarded as model spin-up (i.e. day 0 during 06:00–11:00 UTC). The next 24 h in the model are used to assess the next-day fog (i.e. day 0 at 12:00 to day 1 at 11:00 UTC).

A sensitivity study to CCN activation was carried out through permutations to the CCN and minimum updraft speed. Initial results from the study site showed that CCN could reach up to $500\,\mathrm{cm^{-3}}$ near the surface (Formenti et al., 2019). Thus, the initial CCN number concentration near the surface was increase from 300 to $500\,\mathrm{cm^{-3}}$ (hereafter CCN_500), while the free troposphere was kept at $50\,\mathrm{cm^{-3}}$. CCN_500 has the same vertical profile treatment as CCN_300. Initial concentrations over land and the ocean were the same, as in CCN_300. In another scenario, the mean radius of the CCN was decreased from 0.04 to $0.02\,\mu\mathrm{m}$ as part of a sensitivity analysis (CCN_300_r0.02 hereafter). All other settings were identical to CCN_300. In the final scenario, the minimum updraft speed was increased from 0.01 to $0.1\,\mathrm{m\,s^{-1}}$ (CCN_300_w0.1). This motivation for this scenario was to push the model to a higher CCN activation and see how this effects the size distribution results. For the last scenario, the minimum updraft speed was only assigned in the three lowest vertical levels in the model and should not cause erroneous cloud at higher model levels.

Comparative statistics of model and observed cloud droplet count, LWC, and MVD are presented in the results section. The model grid point that is closest to the site location is extracted for comparison with the observations. A second model grid point, hereafter referred to as "inland", is extracted about 13 km inland when travelling perpendicularly to the coast to demonstrate the dynamics and gradients in the model (Fig. 1b).

2.3 Observations

2.3.1 Meteorology and microphysics

The AEROCLO-sA ground-based field campaign was conducted from 23 August to 12 September 2017 at the University of Namibia campus in Henties Bay ($-22.09495°$ S, $14.2591°$ E; Formenti et al., 2019). The campus is located on the coastline (elevation 20 m a.s.l.) and at the mouth of the non-perennial Omaruru River.

Measurements pertinent to this study include the meteorological measurements of temperature (2 m), relative humidity (2 m), wind speed (10 m), and wind direction (10 m) from a Cimel Electronique compact weather station, part of the PortablE Gas and Aerosol Sampling UnitS (PEGASUS) mobile platform (Formenti, 2020b). Meteorological data were supplemented with atmospheric pressure from the control WRF model simulation described later on. This allowed further variables to be derived, like the water vapour mixing ratio and air density. Radiosonde measured atmospheric profiles of pressure, temperature, relative humidity, wind speed, and wind direction (Formenti, 2020a). Radiosonde were launched form two locations, with one being at the study site and the other being at Jakkalsputz, about 12 km south along the coast of the study site. Visibility measurements were available from a transmissometer with data being recorded every 5 s. The transmissometer is a bistatic system, set up with the emitter and receiver 8.0 m apart and approximately a metre off the ground. The instrument's ana-
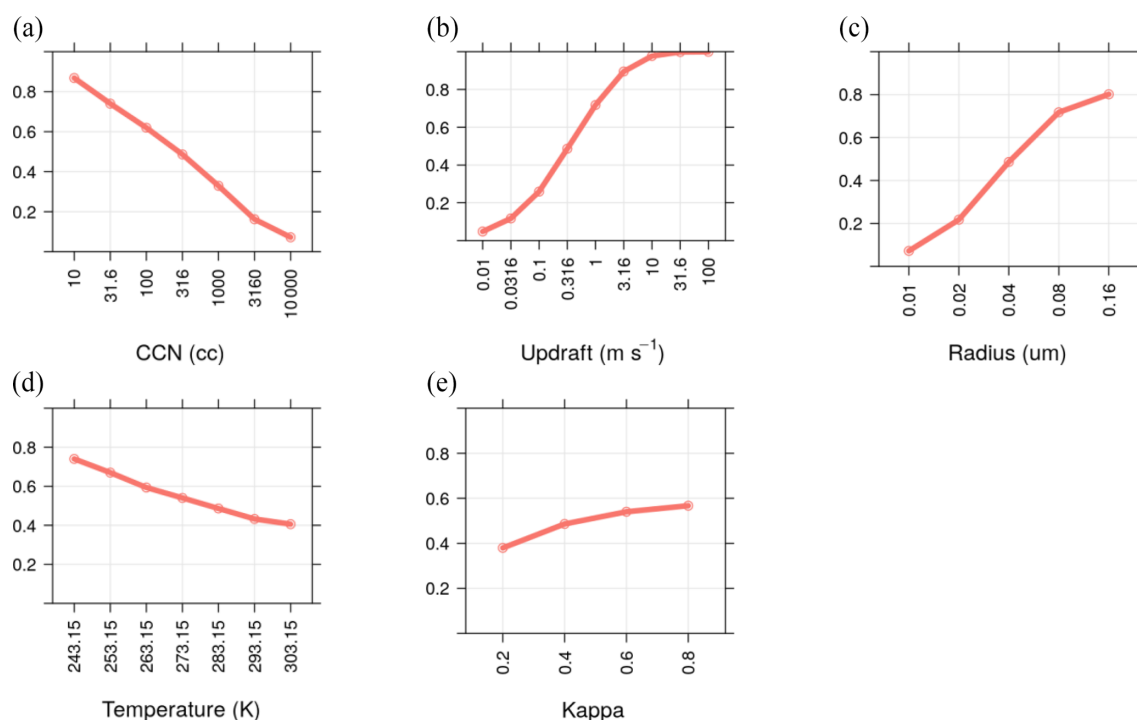
Figure 2. CCN activation look-up table. Activated fraction in response to **(a)** CCN concentration, **(b)** updraft speed, **(c)** CCN radius, **(d)** ambient temperature, and **(e)** kappa (hygroscopicity). For each plot, the remaining four variables are kept constant as follows: CCN is $316 \, \mathrm{cm^{-3}}$, updraft is $0.316 \, \mathrm{m \, s^{-1}}$, radius is $0.04 \, \mu\mathrm{m}$, temperature is $283.15 \, \mathrm{K}$, and kappa is 0.4.

Table 1. WRF model scenarios summary. Updraft refers to minimum updraft speed.

	Scenario	CCN $(\mathrm{cm^{-3}})$	Kappa	Radius $(\mu\mathrm{m})$	Updraft $(\mathrm{m \, s^{-1}})$
1	CCN_300	300	0.4	0.04	0.01
2	CCN_300_landsea	300/100	0.4	0.04	0.01
3	CCN_C10	Colarco et al. (2010)	0.4	0.04	0.01
4	CCN_500	500	0.4	0.04	0.01
5	CCN_300_r0.02	300	0.4	0.02	0.01
6	CCN_300_w0.1	300	0.4	0.04	0.1

logue voltage output response to optical depth (OD) was calibrated using a series of stacked neutral density filters and found to be linear. This voltage was recorded on a Campbell Scientific CR1000 data logger. From the OD, we calculate the extinction coefficient and, hence, visibility using Koschmieder's law. Although this is known to have drawbacks (Lee and Shang, 2016; Nebuloni, 2005), we use the calculated visibility in a qualitative sense in this study.

Cloud droplet measurements were conducted with a fog monitor 100 (FM-100) providing droplet number concentration, size distribution, and liquid water content for particle sizes with optical equivalent diameter of 1 to 50 µm. This instrument is a forward-scattering spectrometer probe, where the droplet size is calculated based on scattered light from a laser and employing the Mie theory (Spiegel et al., 2012).

The particle is assumed to be spherical and made of water with a known refractive index. Droplets in the size range 2–50 µm can be counted with bin sizes between 2 and 3 µm. The instrument was calibrated with glass beads of known diameter and refractive index. The LWC is calculated based on the assumption that each droplet is spherical. Data were recorded every second and later aggregated to 1 min averages.

A cloud condensation nucleus (CCN) counter (mini-CCNC) was deployed at the site. The supersaturation during data capture was set to scanning mode, meaning that supersaturation varied between 0.1 % and 0.7 %. The CCNC was calibrated prior to the campaign using ammonium sulfate to determine the relationship between the temperature gradient along the column and the effective supersaturation. A wide wind-oriented intake facilitated airflow into the instrument

and total CCN was recorded at a high frequency (every second).

2.3.2 Activated CCN

Activated CCN, the percentage of hygroscopic CCN that are present as cloud droplets as described in the model microphysics section, can be estimated as measurements of cloud droplets (from FM-100) and CCN (from mini-CCNC) are co-located. This definition is maintained in the processing of the observations to allow for consistency in comparing the model microphysics scheme with observations. Data overlap from these instruments coincided with a fog event on 9 September 2017, which was used to estimate the activated CCN at the site. The CCN counter cycled through supersaturation from 0.1 % to 0.7 % to account for varying aerosol sizes. For our purposes, CCN data were subset to supersaturation range from 0.098 % to 0.151 %. Practically, this means that CCN data are available at about 3 min intervals due to the supersaturation cycle of the instrument. The 1 s data were then averaged to 1 min for both the CCN and FM-100 and paired according to matching times. CCN concentration is expected to be underestimated during wet conditions due to the design of the inlet on the instrument. To overcome this, we use the CCN concentration in the period prior to fog in the activated CCN calculation. A period of 1 h of observations when visibility was 10 km prior to fog formation was used as the CCN sample. This period occurred from 01:00 to 02:05 UTC on 9 September 2017. The average CCN concentration was calculated for this period and used in conjunction with the N_t during fog conditions to calculate activated CCN as N_t / CCN (cm^{-3}). Lastly, the data were filtered for conditions where Vis < = 1 km (based on the World Meteorological Organization, 2008, definition) and $N_t > 25$ cm^{-3}, where the visibility threshold meant that fog conditions were represented, and the N_t threshold was estimated as being representative of a baseline in the fog monitor.

2.3.3 Satellite

The spatial evolution of the cloud and fog is presented using the Spinning Enhanced Visible and Infrared Imager (SEVIRI) from Meteosat Second Generation 3 (MSG-3; Schmetz et al., 2002). MSG3, also known as the Meteosat 10 satellite, is in a geostationary orbit over 9.5° E. Nighttime scenes are false colour composite images using the night microphysical product from EUMETSAT (European Organization for the Exploitation of Meteorological Satellites; Eumetsat, 2009). This product is a red–green–blue (RGB) composite, where the red channel is the difference between 12.0 and 10.8 μm channels (linear stretch −4 to 2 K), green is the difference between 10.8 and 3.9 μm channels (linear stretch 0 to 10 K), and blue is the 10.8 μm channel (linear stretch 243 to 293 K). Daytime scenes are an RGB of the visible channels (R is VIS 06; G is VIS 0.8; B is IR 1.6).

3 Results and discussion

3.1 Case study description

There were two fog events observed on consecutive days on 9 and 10 September 2017 (hereafter case 1 and case 2, respectively) during the AEROCLO-sA campaign at Henties Bay (Fig. 3). Visibility dropped below 1 km from about 03:00 to 07:00 UTC during case 1. The wind direction was predominantly northwesterly and veering to northeasterly during these days, which is in contrast to the dominant wind direction of southwesterly during the full campaign dates. Wind speed was 2 m s^{-1} or less during the events. Water vapour mixing ratio ranged between 8 and 10 g kg^{-1} during the fog events but was more than 10 g kg^{-1} during the day. The observed relative humidity remained over 90 % throughout the case study period. A temperature inversion with a strength of about 10 °C was present on both mornings below 1000 m a.s.l. Satellite images for case 1 indicate an isolated cloud over the study site from 00:00 UTC, and by 03:00 UTC, the fog patch is elongated along the coastline (Fig. 4). No cloud is present over the ocean, and this fog patch is not associated with a stratus deck. For case 2, visibility dropped below 1 km from 04:00 to 07:00 UTC. Satellite images indicate that cloud was present over the site from 16:00 UTC the day before and was associated with stratus over the ocean (Fig. 5). This cloud gradually advected over the land, and by 21:00 UTC, the visibility had decreased to 2 km. By 03:00 UTC, just before fog onset, the stratus deck had increased extent over the ocean. After sunrise, the cloud over the land dissipated, while the cloud over the ocean remained through the day and into the following night.

3.2 Activated CCN

The activated CCN calculated from the observations, as described in Sect. 2.3.2, ranged from 0.058 to 1 (i.e. 5.8 % to 100 %), where 1 is the theoretical maximum (Fig. 6). The median (mean) was 0.55 (0.56), and the standard deviation was 0.24. When the fog was most dense, represented by the highest N_t values between 06:30 and 07:15 UTC, the activated CCN reached over 80 %. Values of CCN activation of 0.8 at 0.1 % supersaturation are possible and have been observed (Che et al., 2016). When considering the CCN activation look-up table from WRF (Fig. 2), an updraft speed of 0.1 m s^{-1} corresponds to CCN activation just below 0.3. Therefore, assigning a minimum updraft speed of 0.1 m s^{-1} can be a reasonable assumption, as it falls within the median of activation at the site 0.56.

3.3 Analysis of simulations

3.3.1 Evaluation of simulated meteorology

The observed daily temperature range at the study site is narrow and did not exceed 5 °C, which is a clear indication of
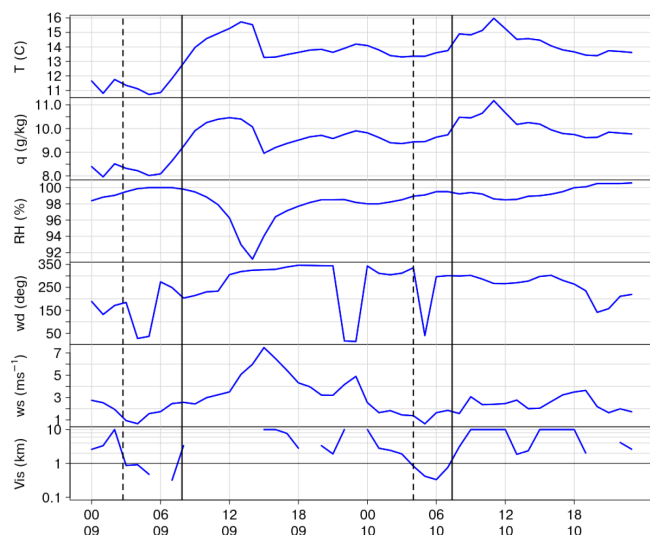
Figure 3. Meteorological variables from the Cimel Electronique compact weather station at the site during the two fog events on 9 and 10 September 2017. The variables are temperature (T in degrees Celsius), water vapour mixing ratio (q), relative humidity (RH), wind direction (wd), wind speed (ws), and visibility (Vis) from the transmissometer. Vertical black dashed (solid) lines indicate fog start (end) times. The x axis shows hours in UTC (site is UTC+2) and the day of the month in September.

the maritime influence on modulating temperature (Fig. 7a). The modelled diurnal temperature range is larger and more representative of a terrestrial site, with the maximum temperature being 4–5 °C warmer and the minimum between 1–5 °C colder than observed. The combination of model horizontal resolution and physics may be limited to resolve the exact location of the land–sea interface occurring at the sampling site, which is within 200 m of the sea shore. Consequently, the cold bias may trigger early saturation, as suggested by the relative humidity time series in Fig. 7e. The water vapour mixing ratio is underestimated by 2 to 4 g kg^{-1} during the nighttime, but this is not dry enough to prevent saturation. Simulated wind speed is within 1 m s^{-1} for most of the simulation and, more importantly, during the observed fog periods (Fig. 7b). However, the maximum bias is 2 m s^{-1} (negative) during the night of 8 September, and the model underestimated the daytime wind speed on 9 September by approximately 2 m s^{-1}. The observed wind direction shifts from southwesterly on 8 September to northerly during the case studies. The simulation captures this progression, although the model shifts back to southerly during the day of 9 September (coinciding with the underestimated maximum wind speed) before veering back to northerly.

The modelled profiles of temperature and relative humidity displayed the low level inversion and moisture, as seen in the observed profiles. For case 1, the model captured the near-surface temperature inversion at about the same height (base of inversion is at $\sim$ 250 m) and strength ($\sim$ 10 °C) as

the observed inversion (Fig. 8). Subsequently, the moisture and associated relative humidity was over 80 % near the surface and decreased rapidly from the base of the inversion to 10 % at around 600 m. It is worth noting that the observed relative humidity at the surface was below 100 % and peaked near 100 % at about 250 m, while the model was at 100 % at the corresponding heights. For case 2, the base of the observed temperature inversion was higher at about 800 m and coincided with the peak relative humidity of 100 % (Fig. 9). The model inversion height was also higher than case 1 model results but was still below 500 m. The reason for the higher inversion level during case 2 is not clear. This could be attributed to the difference in timing of the sonde (1 h later) or that the fog event is optically thick and has a major effect on the radiation (as in Price, 2011; Boutle et al., 2018). Nevertheless, the model is capturing a low level surface inversion trapping the moisture below this inversion, as in the observations.

3.3.2 Spatial distributions of CCN and cloud droplet concentration

The initial CCN concentration for CCN_300 is similar over land and ocean (Fig. 10a). However, over time, the concentration over the ocean is relatively higher than over the land, as is evident in the mean concentration in Fig. 10b. This is counter-intuitive, as observed CCN concentrations are typically lower over the ocean than the land (Seinfeld and Pandis, 2016). The relative decrease in concentration over the land is most likely due to the treatment of the vertical distribution of CCN in the scheme, where CCN concentrations have a steeper decrease with height when terrain height is above 1000 m. This allows for the dilution of the surface CCN concentration during vertical mixing of the atmosphere. Furthermore, the boundary conditions for scenario CCN_300 had relatively lower concentrations of CCN than the ambient CCN in the domain. This explains the lower CCN concentrations over the southern part of the ocean in the domain as clean air was advected from the boundary conditions.

The initial CCN concentration for scenario CCN_300_landsea shows a clear contrast, with lower concentration over the ocean than the land (Fig. 10c). The lower concentration over the ocean counteracts the accumulation of CCN over time, as seen in CCN_300, resulting in a more balanced mean CCN concentration between land and ocean (Fig. 10d). Scenario CCN_C10 has an order of magnitude higher for the concentration of CCN (Fig. 10e and f) and does exhibit higher concentrations over land than the ocean. This contrast is maintained though out the simulation as the terrain-dependent vertical profile described earlier is not applied to these CCN. Furthermore, as the CCN are a subset of a larger data set, the boundary conditions include similarly higher concentrations of CCN, and clean air is not advected into the domain.
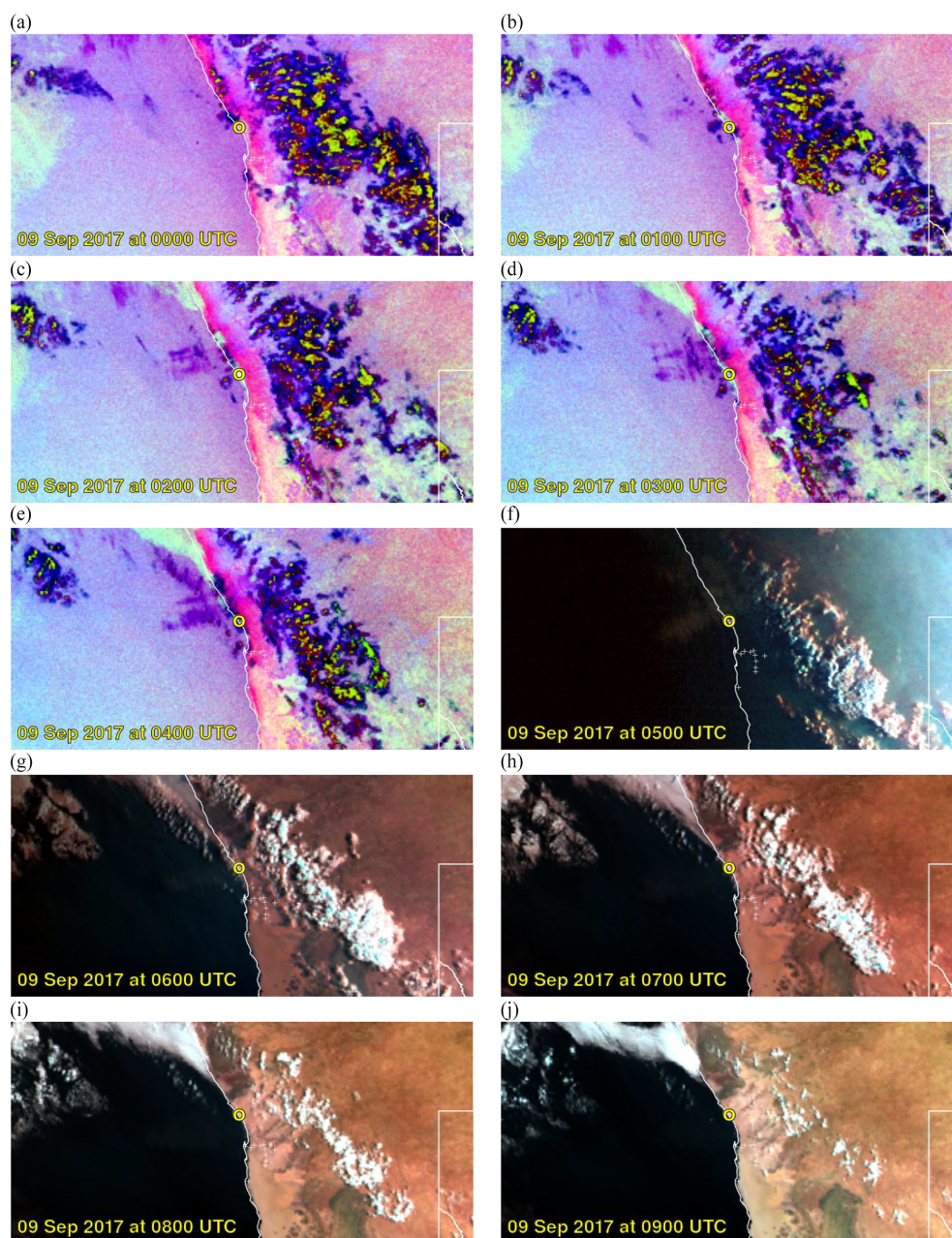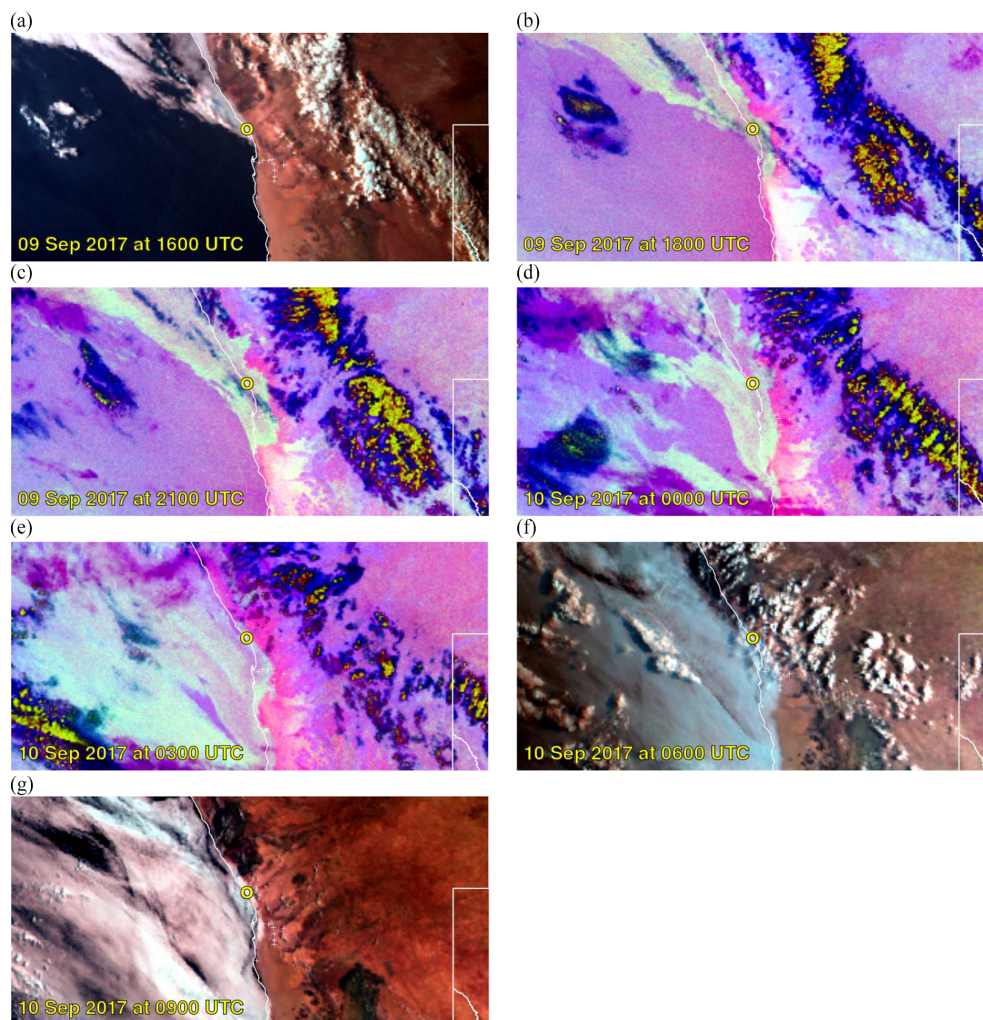
Figure 4. SEVIRI images of night microphysical RGB product **(a–e)** and day visible channels **(f–j)** for the fog event on 9 September 2017. The yellow open circle is the study site. The site is UTC+2. The extent matches the WRF model 3 km domain, which extends 1386 km (east–west) by 720 km (north–south).

The evolution of CCN concentration for CCN_300 during case 2 is shown in Fig. 11. It clearly shows that, by 12:00 UTC (forecast hour 7), the concentration over the ocean is higher (500–600 cm^{-3}) than over the land in the lowest model level. The clean air from the boundary conditions is evident in the south and continues to propagate through the domain throughout the forecast. Ahead of this advection, concentration increases as CCN are transported from the south and accumulate. An onshore flow of CCN onto the low-lying Namib desert is also evident. At Henties Bay, the wind direction is southwesterly (200°) from 12:00 to 18:00 UTC and veers to northwesterly (300°) from about 19:00 to 06:00 UTC. This northwesterly flow allows for the low level transport of the accumulated CCN back along the coastline.

The fog onset, represented by cloud droplet concentration, is shown in Fig. 12, where droplet concentration reached up to 50 cm^{-3}. Over land, fog starts to form along the coast first

Figure 5. SEVIRI images of night microphysical RGB product **(b–e)** and day visible channels **(a, f, g)** for the fog event on 10 September 2017. The yellow open circle is the study site. The site is UTC+2. The extent matches the WRF model 3 km domain, which extends 1386 km (east–west) by 720 km (north–south).
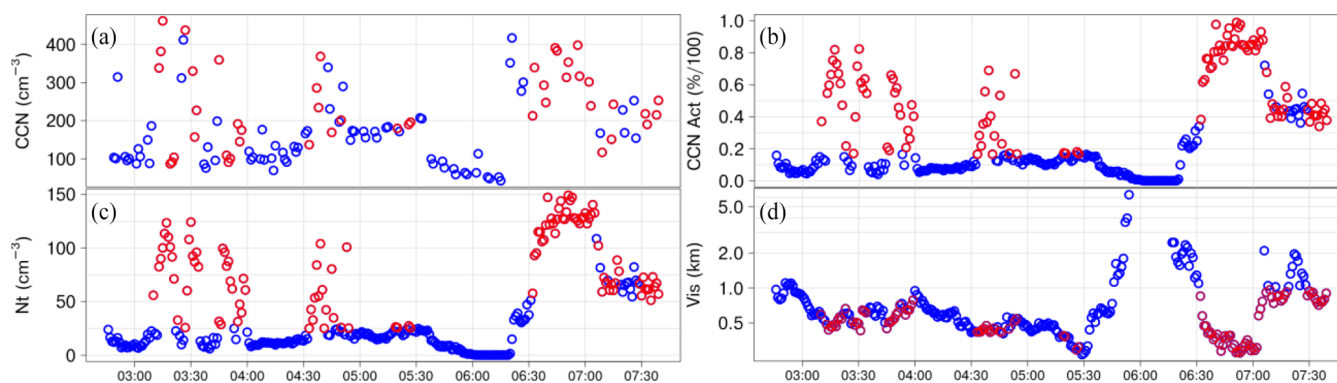
Figure 6. Time series of **(a)** CCN (cm^{-3}), **(b)** N_t (cm^{-3}), **(c)** activated CCN (proportion), and **(d)** visibility during the fog event on 9 September 2017. Red dots indicate data points used to calculate activated CCN. Blue dots are not used to calculate activated CCN and are shown for context. Times are in UTC (site is UTC+2).
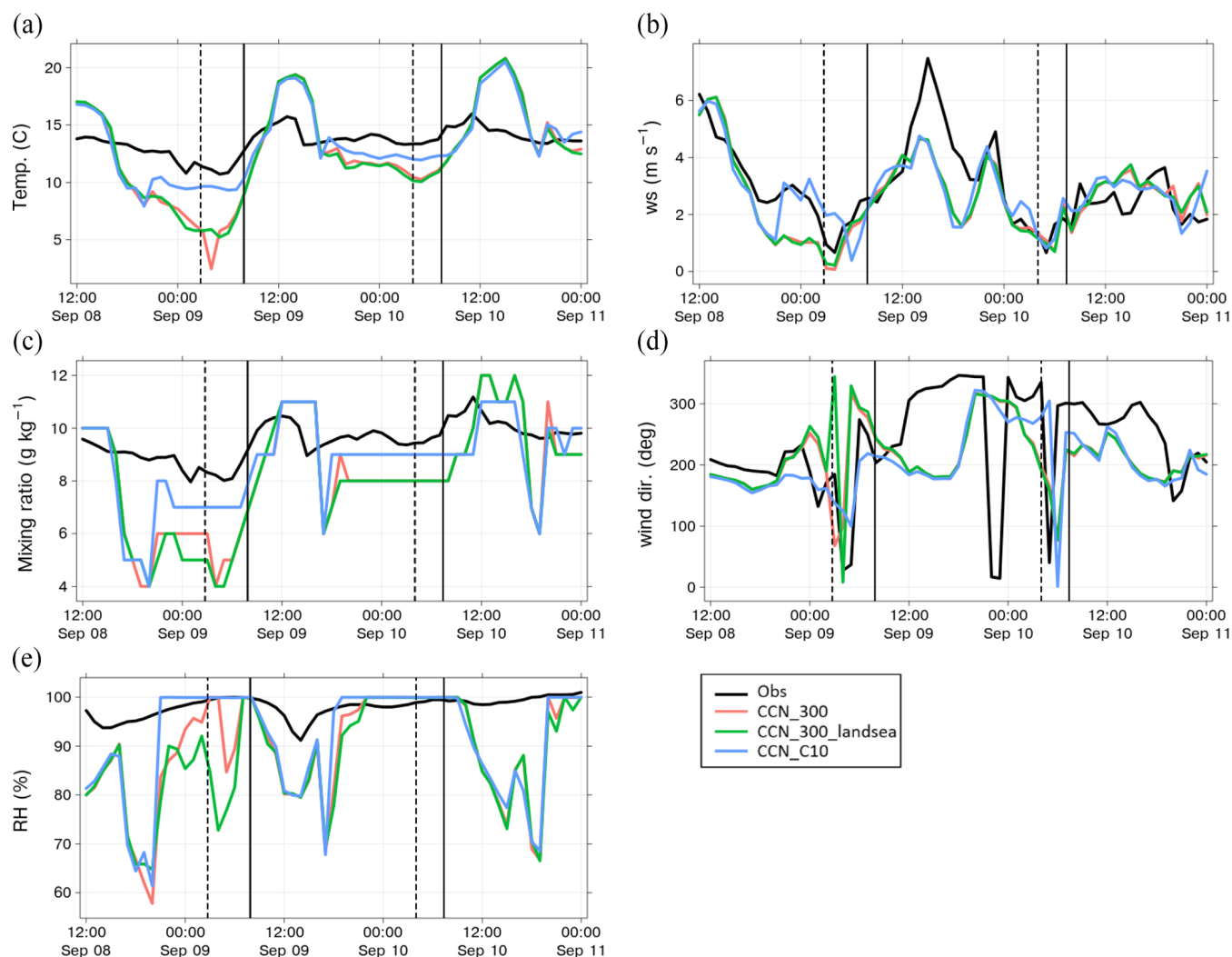
Figure 7. Time series of model and observed meteorological variables at Henties Bay for **(a)** temperature, **(b)** wind speed, **(c)** water vapour mixing ratio, **(d)** wind direction, and **(e)** relative humidity. Times are in UTC (site is UTC+2).

and then extends further inland, signifying that the simulated fog is due to advection and not to radiation. Radiation fog would be expected to form inland first, or simultaneously with coastal fog, as the radiative cooling should be stronger inland (e.g. Weston and Temimi, 2020). The fog reached maximum inland extent at 04:00 UTC (Fig. 13a) before dissipating inland by 07:00 UTC (Fig. 13d). Cloud droplets are present over the ocean from 21:00 to 07:00 UTC. The spatial distribution of CCN and cloud droplet concentration for CCN_300_landsea were similar to CCN_300, although the concentrations were generally lower.

The evolution of CCN concentration for CCN_C10 during case 2 is shown in Fig. 14. What is notable is the lack of clean air advection from the boundary conditions, the relative contrast in concentration between land and ocean is maintained throughout, and there is generally less variation over time compared to CCN_300. However, the onshore flow and

mixing of marine CCN in the Namib desert is still evident, meaning that the study site is influenced by the marine CCN during these simulations.

Fog onset over the land is similar to CCN_300, as this is controlled by the ambient conditions. However, cloud droplet concentration is 2 to 3 times higher in general compared to CCN_300, reaching up to $150\,\mathrm{cm}^{-3}$ (Fig. 15). Even though the percentage of droplet activation decreases as CCN concentration increases (Fig. 2a), the initial CCN is significantly high enough to activate more cloud droplets than CCN_300. As in CCN_300, cloud droplets are present over the ocean from 21:00 to 07:00 UTC. The maximum fog extent over the land (Fig. 16) is a good match to the satellite data (Fig. 5).

In general, the first three scenarios did well in capturing the fog extent over the land. They show the cloud forming at the coast first before moving inland, suggesting that the dynamics of the formation are captured in the model. Over the
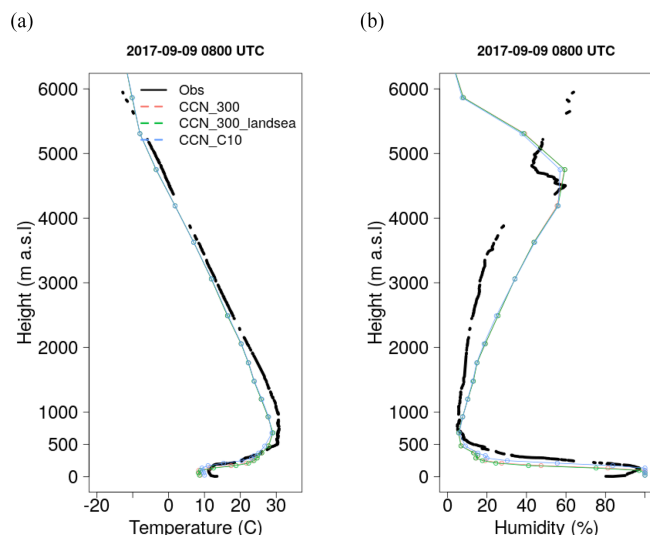
(a)

(b)

Figure 8. Radiosonde profiles of (a) temperature and (b) relative humidity from Jakkalsputz on 9 September 2017. The sonde was launched at 07:50 UTC, and the model is from 08:00 UTC. The site is UTC+2.
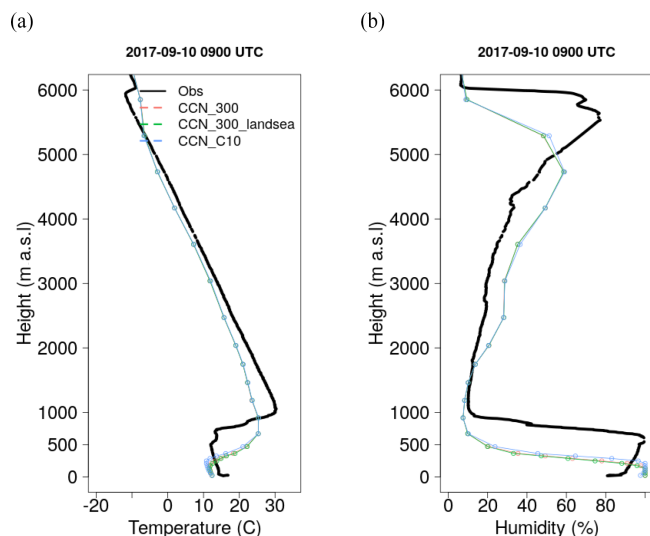
(a)

(b)

Figure 9. Radiosonde profiles of (a) temperature and (b) relative humidity from Jakkalsputz on 10 September 2017. The sonde was launched at 09:10 UTC, and the model is from 09:00 UTC.

ocean, cloud droplet activation is overactive, as a cloud deck is present from 21:00 UTC (Figs. 12 and 15a). At night, the air over the ocean is saturated (not shown), which we assume is from either a cold bias or positive bias in the water vapour mixing ratio. Saturation is the first condition that must be met for droplet activation, and it is assumed this is causing a persistent cloud deck over the ocean. The cloud deck was also present in case 1 simulations, while the satellite shows no cloud is present over the ocean. It has been demonstrated now that, in all scenarios, there is a contrast between the land and

ocean in terms of CCN and cloud droplet concentrations. Additionally, the semi-permanent cloud deck in the simulations impinges onto the adjacent land, mainly due to the onshore flow. Similar patterns of excess frequency of cloud cover (by 30 % to 50 %) over the ocean were reported for a regional climate model simulation over Namibia (Haensler et al., 2011). They demonstrate the same high contrast between ocean and land and highlight that the study sites at the coast fall within a transition zone in the model. The study site is located at the interface between these two contrasting conditions and falls within the impingement zone of the simulations. This must be kept in consideration when comparing the model microphysics to the observations from the site, which will be discussed in the following section.

3.3.3 Comparison of simulated and observed fog microphysics

The observed microphysics during case 1 showed cloud droplet number concentrations of up to $150 \, \mathrm{cm^{-3}}$ (mean of $42 \, \mathrm{cm^{-3}}$), maximum LWC around $0.25 \, \mathrm{g \, m^{-3}}$, and MVD up to $27 \, \mu\mathrm{m}$ (Fig. 17a–c). Case 2 demonstrated a higher mean number concentration of $79 \, \mathrm{cm^{-3}}$, LWC peaked at $0.3 \, \mathrm{g \, m^{-3}}$, and MVD was lower up to $21 \, \mu\mathrm{m}$.

During case 1, the cloud droplet number concentration was below $25 \, \mathrm{cm^{-3}}$ for CCN_300, approximately 6 times less than the observations. However, the LWC was comparable to the observations at about $0.2 \, \mathrm{g \, m^{-3}}$. This means that the LWC is distributed among fewer droplets than the observations and that the DSD will shift towards larger droplet diameters, which is evident in the MVD around $30 \, \mu\mathrm{m}$. The model exhibited larger number concentrations during case 2, which appears to be associated with higher CCN concentrations (Fig. 17d). This, in turn, results in marginally increased LWC and an associated decrease in the MVD. As expected, CCN_300_landsea was similar to CCN_300 but with lower cloud droplet concentrations due to lower CCN concentrations. The CCN concentrations were within the observed mean CCN concentration, which could be a good starting point for sensitivity tests on percentage droplet activation for the future. The modelled updraft speed at the site was low, i.e. below $0.02 \, \mathrm{m \, s^{-1}}$ prior to fog formation and either negative or below $0.01 \, \mathrm{m \, s^{-1}}$ during fog (Fig. 17e). This means that the applied updraft speed is the minimum updraft speed from Table 1 when the microphysics is activated.

The scenario CCN_C10 has around 10 times higher initial concentrations of CCN throughout the simulation. This resulted in cloud droplet concentrations around $125 \, \mathrm{cm^{-3}}$ during case 1 and case 2, which was comparable with the observations. Case 2 was marginally lower than case 1 in this simulation, as the CCN were lower. The maximum LWC during case 1 was about the same as the observed at $0.25 \, \mathrm{g \, m^{-3}}$ and just over $0.3 \, \mathrm{g \, m^{-3}}$ during case 2. As the cloud droplet number concentration and LWC are comparable to the observations, the MVD was much closer, with a maximum around
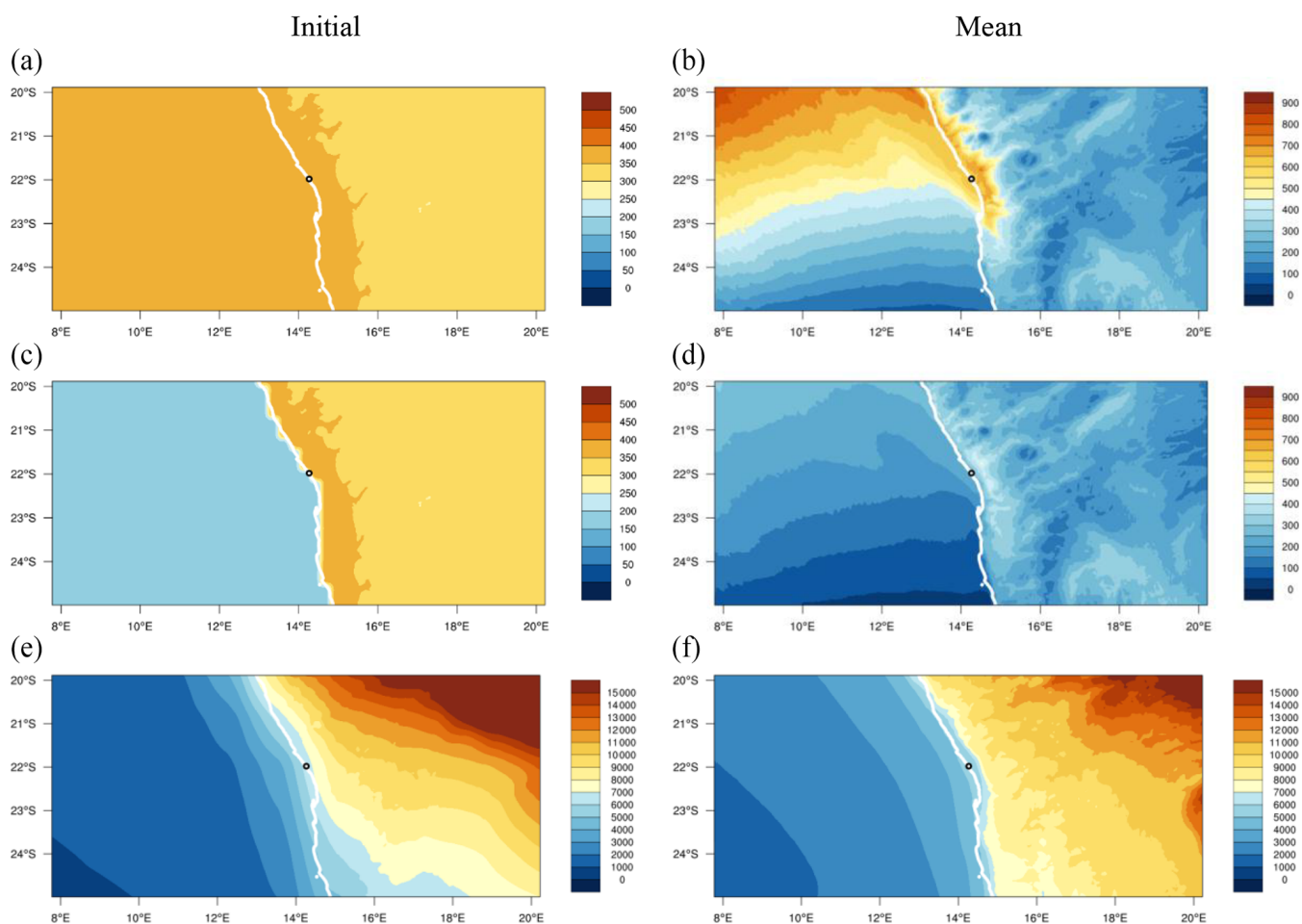
Figure 10. Initial and mean water-friendly CCN concentration (cm^{-3}) for scenarios **(a, b)** CCN_300, **(c, d)** CCN_300_landsea, and **(e, f)** CCN_C10. Note the different scale in panel **(c)**. The black dot is Henties Bay.

20 μm for both cases. This scenario demonstrated the best performance in terms of cloud microphysics at the site, which is interesting as the initial CCN values appear to be largely overestimated. The reported mean of CCN at the site ranged from 230–550 cm^{-3} (Formenti et al., 2019), while the modelled CCN was above 4000 cm^{-3} throughout the simulation. As presented in Sect. 3.2, the observed CCN activation can be between 20 % and 80 % during fog events, while the modelled activation is much lower, at around 10 %. To understand this further, we need to discuss CCN activation in the model scenarios.

CCN activation is most sensitive to CCN concentration and then updraft speed. For each scenario, the CCN concentration is always present and does not vary greatly. Keep in mind that the mean radius and kappa values are constant throughout.

The updraft speed during both cases was negative, meaning that the minimum updraft of 1 cm s^{-1} is applied. If we consider case 2, we can see that the saturation is met at 18:00 UTC, and droplets are formed prior to the fog event

(Fig. 17a). From this point, droplets persist or are activated whenever saturation is met until the case 2 event. The potential drawback of using the updraft velocity to define drop activation for fog formation has been discussed previously (Boutle et al., 2018; Poku et al., 2019). The argument is that fog often forms under stable conditions when no updraft is present and that activation is instead due to the cooling of the air. In addition, the threshold updraft speed is often higher than the 0.01 m s^{-1} used in the T14 scheme, which effectively results in a higher supersaturation and excess droplet activation than would be expected for a fog event (Boutle et al., 2018; Poku et al., 2019). Reported activation fractions of CCN in fog are around 20 % but reach up to 40 % (Mazoyer et al., 2019). To some extent, the implementation of a relatively low updraft speed in the look-up table mitigates against excess droplets forming in the T14 scheme. Activation at speeds less than 0.03 m s^{-1} are around 10 % or less. Thompson and Eidhammer (2014) acknowledge the use of updraft speed as a potential limitation in the scheme in terms of fog formation. Their proposed workaround is to include
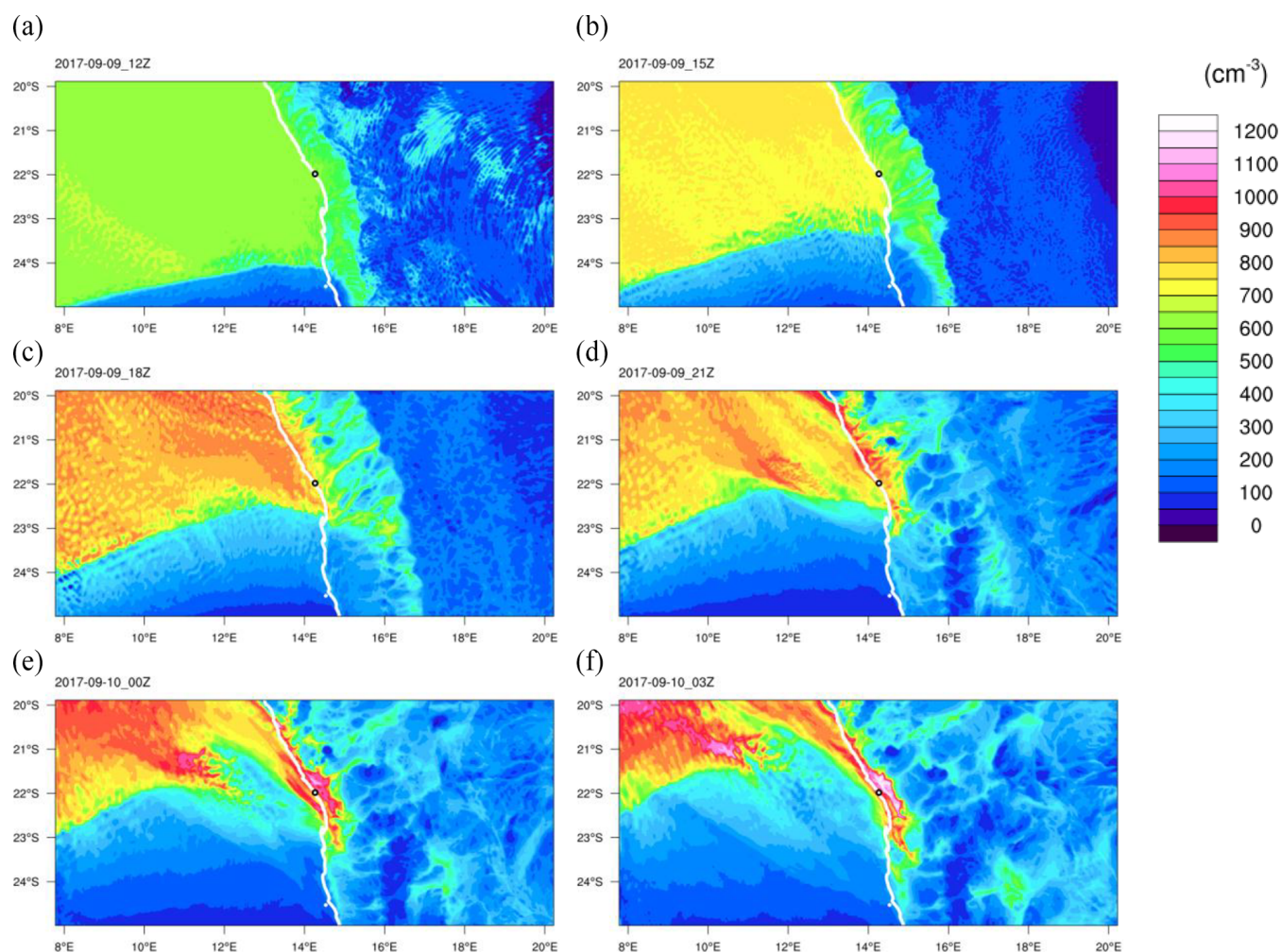
(a)
(b)

(c)
(d)

(e)
(f)

Figure 11. Evolution of water-friendly CCN concentration (cm^{-3}) for the event on 10 September 2017 for scenario CCN_300. The black dot is Henties Bay. Time is in UTC (site is UTC+2).

cooling tendency as proxy for updraft speed and then assigning a speed that will activate the appropriate number of droplets. This may come with a new set of problems in terms of early activation, but this remains to be seen.

The observed DSD needs to be transformed to a gamma distribution in order to compare it to the model. This is possible as the only inputs to the shape and slope parameters are the number concentration and LWC (Eqs. 2 and 3). The mean number concentration and LWC for each case was used, and the transformation of the observed (Obs_raw) and gamma distribution (Obs_gamma) can been seen in Fig. 18. While the observations show signs of a trimodal distribution with peaks around 7, 16, and 30 µm, the gamma distribution has one peak at around 11 µm. The three modes in the observed distribution could be representative of the various CCN populations, where larger salt particles with higher kappa values could represent the largest mode, while the smaller sulfates represent the smaller modes. Droplet growth by collision and coalescence can be another explanation for the

larger droplets and spectrum widening in a maturing cloud (e.g. Egli et al., 2015; Mazoyer et al., 2019). From the model scenarios, CNN_C10 demonstrates the best match with the observations (Fig. 19), with the best performance in case 2. For the scenarios where initial CCN is constant, the distribution shifts to larger droplet sizes.

The results of the sensitivity analysis are discussed below. The influence of number concentration on LWC and MVD is further highlighted by the CNN_500 scenario. For all times, this scenario has higher cloud droplet concentrations that CCN_300 (Fig. 20a). This results in overall higher LWC and lower MVD (Fig. 20b and c). The inverse is shown with scenario CNN_300_r0.02. In this scenario, the radius of the CCN was halved, which results in a lower number of activated droplets, according Kohler theory (Fig. 2b). Similar sensitivity analyses have been reported by Poku et al. (2019) and Stolaki et al. (2015). The most interesting results comes from scenario CCN_300_w0.1, which demonstrated the closest match to the observed number concentra-
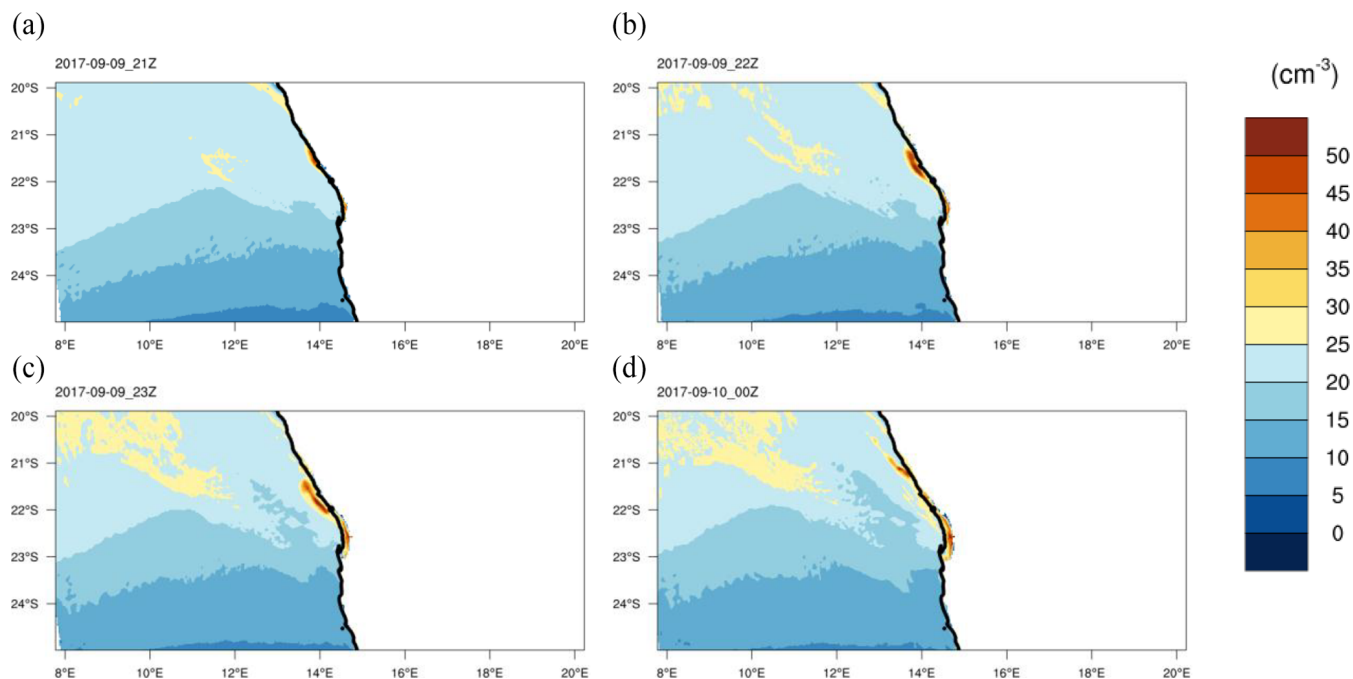
Figure 12. Cloud droplet concentration (cm^{-3}) onset for the event on 10 September 2017 for scenario CCN_300. The black dot is Henties Bay. Time is in UTC (site is UTC+2).
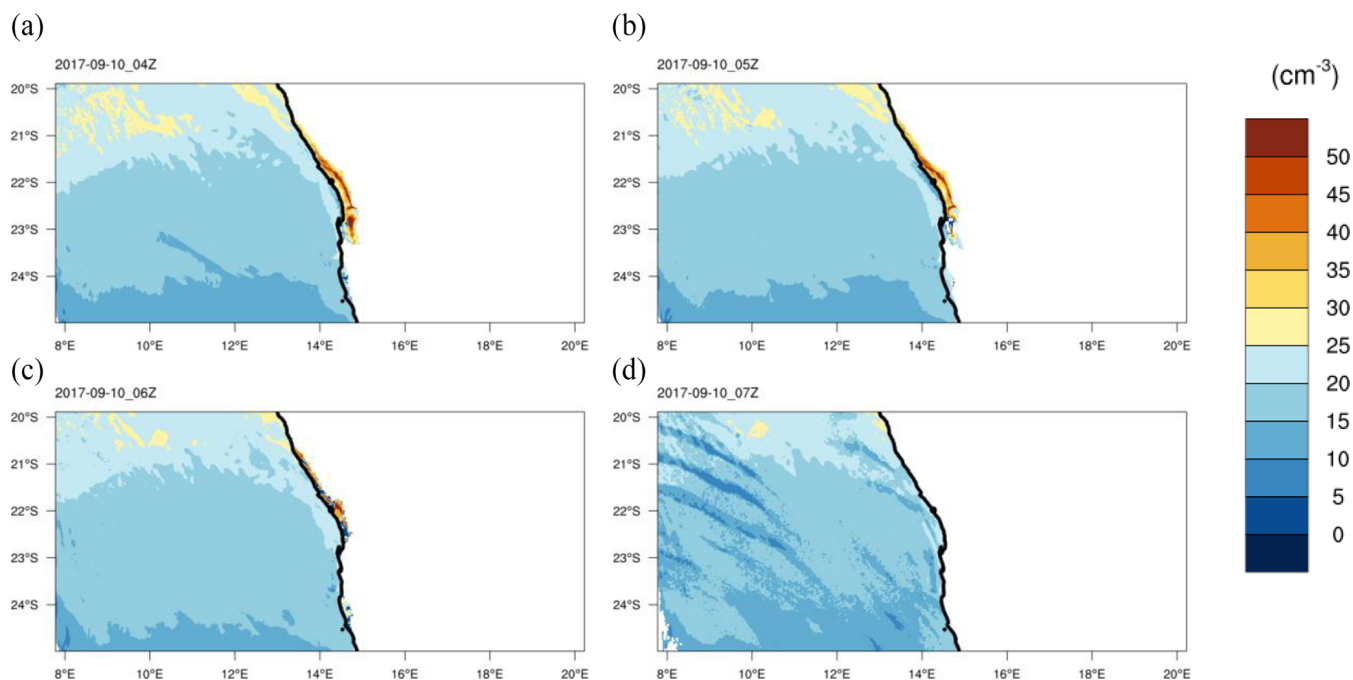

Figure 13. Cloud droplet concentration (cm^{-3}) during maximum extent and highest concentration for the event on 10 September 2017 for scenario CCN_300. Maximum extent was at **(a)** 04:00 UTC and maximum concentration at Henties Bay was at **(d)** 07:00 UTC. The black dot is Henties Bay.
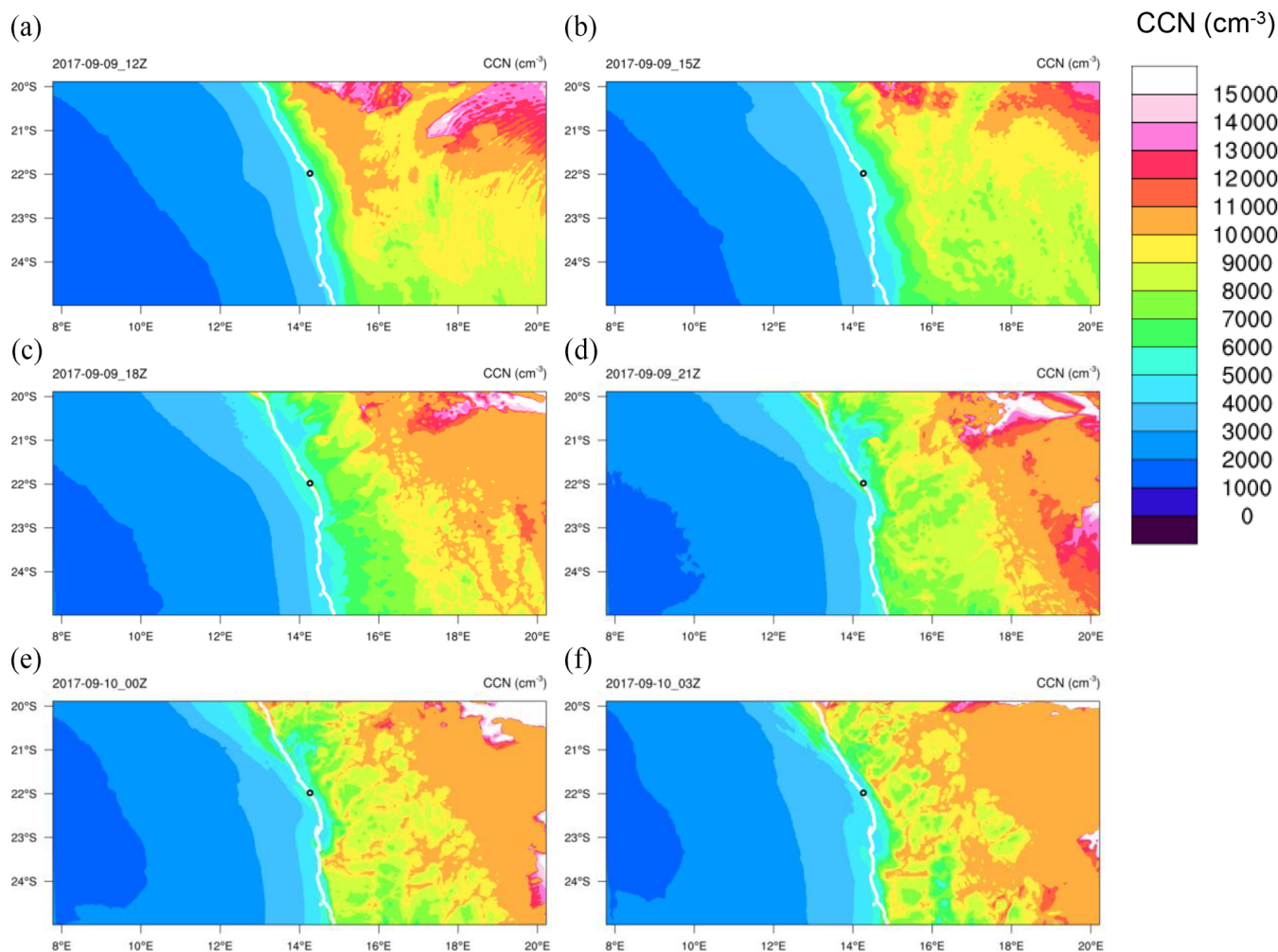
Figure 14. Evolution of CCN concentration for the event on 10 September 2017 for scenario CCN_C10. The black dot is Henties Bay.

tion, LWC, and MVD. The logic behind this scenario was to increase the number of activated droplets by increasing the minimum updraft speed from 0.01 to $0.1 \, \mathrm{m \, s^{-1}}$, which should allow around 30 % activation. Here we have a scenario in which both the CCN and cloud droplet number are in line with the observations. This follows on from the discussion of using temperature tendency as a proxy for updraft speed, showing that it could work if the nucleation percentage is known and an appropriate updraft speed is assigned. However, in our case, the minimum updraft speed of $0.1 \, \mathrm{m \, s^{-1}}$ may relate to an unrealistic cooling rate for this fog event, which we discuss below.

An updraft speed of $0.1 \, \mathrm{m \, s^{-1}}$ equates to a cooling rate of $3.51 \, \mathrm{K \, h^{-1}}$ ($2.34 \, \mathrm{K \, h^{-1}}$) at the dry (wet) adiabatic lapse rate. Our observed cooling rate at 2 m air temperature is below $1 \, \mathrm{K \, h^{-1}}$ prior to the fog formation (Fig. 3). A cooling rate of $1 \, \mathrm{K \, h^{-1}}$ equates to an updraft speed between 0.028 and $0.04 \, \mathrm{m \, s^{-1}}$ at the dry and wet adiabatic, respectively. The modelled updraft speed is below $0.02 \, \mathrm{m \, s^{-1}}$ prior to fog formation and therefore in line with the observed cooling rate.

Therefore, the use of a minimum updraft speed of $0.1 \, \mathrm{m \, s^{-1}}$ does not have a physical basis in our simulation and is used only as part of the sensitivity analysis. It is also clear that if we use a physical basis for the minimum updraft speed, then the model will not activate enough cloud droplets and that another physical process must be manifesting the droplet activation.

In our case, we assume that the observed fog events are due to cloud base lowering (CBL). The satellite images in Figs. 4 and 5 indicate that cloud is present over the site before fog is observed in the surface observations (Fig. 3). The surface observations indicate that fog starts at 02:43 and 04:00 UTC on 9 and 10 September, respectively (Fig. 3). Cloud is visible from the satellite from 01:00 UTC on 9 September and even 16:00 UTC on 9 September prior to the fog on 10 September. From the literature, cloud base lowering fog events do not show the same cooling rate at the surface as radiation fog, as the overhead cloud inhibits cooling (e.g. Román-Cascón et al., 2019). Furthermore, the influence of the maritime environment at the site will dampen cooling from the desert
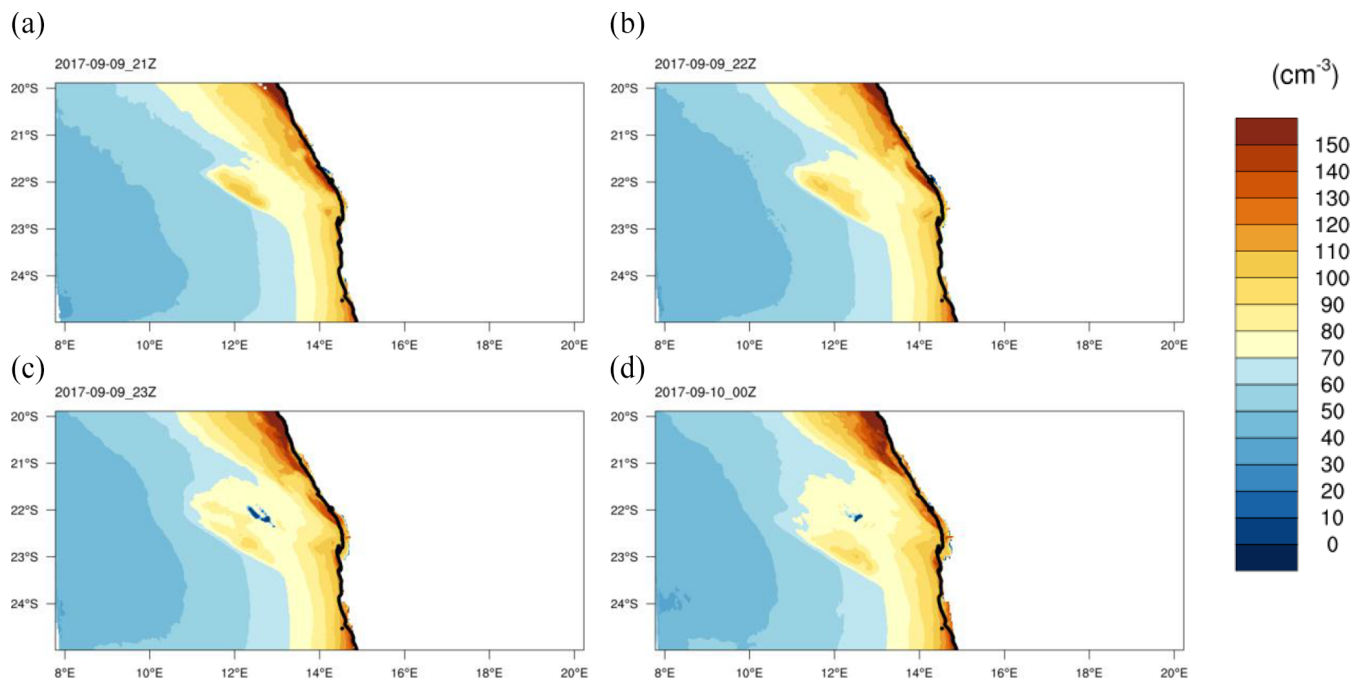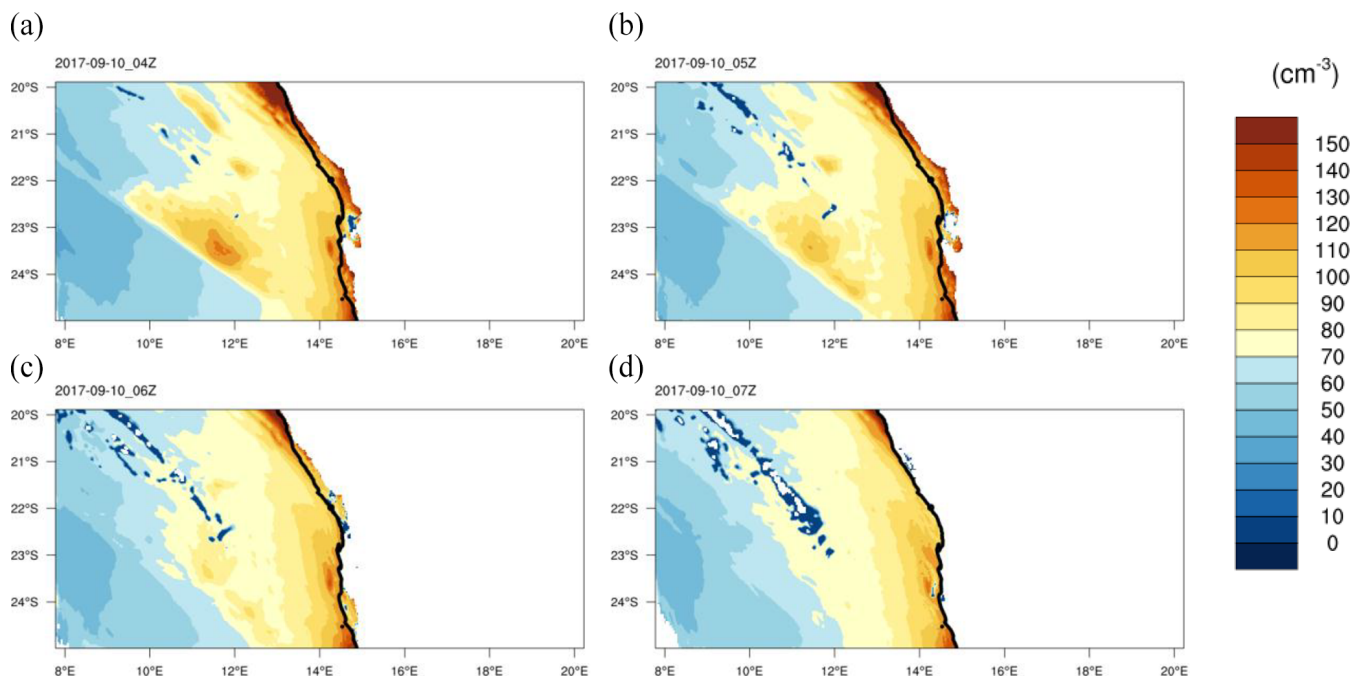
Figure 15. Cloud droplet concentration (cm^{-3}) onset for the event on 10 September 2017 for scenario CCN_ C10. The black dot is Henties Bay.

Figure 16. Cloud droplet concentration (cm^{-3}) during maximum extent and highest concentration for the event on 10 September 2017 for scenario CCN_C10. Maximum extent was at **(a)** 04:00 UTC and maximum concentration at Henties Bay was at **(d)** 07:00 UTC. The black dot is Henties Bay.
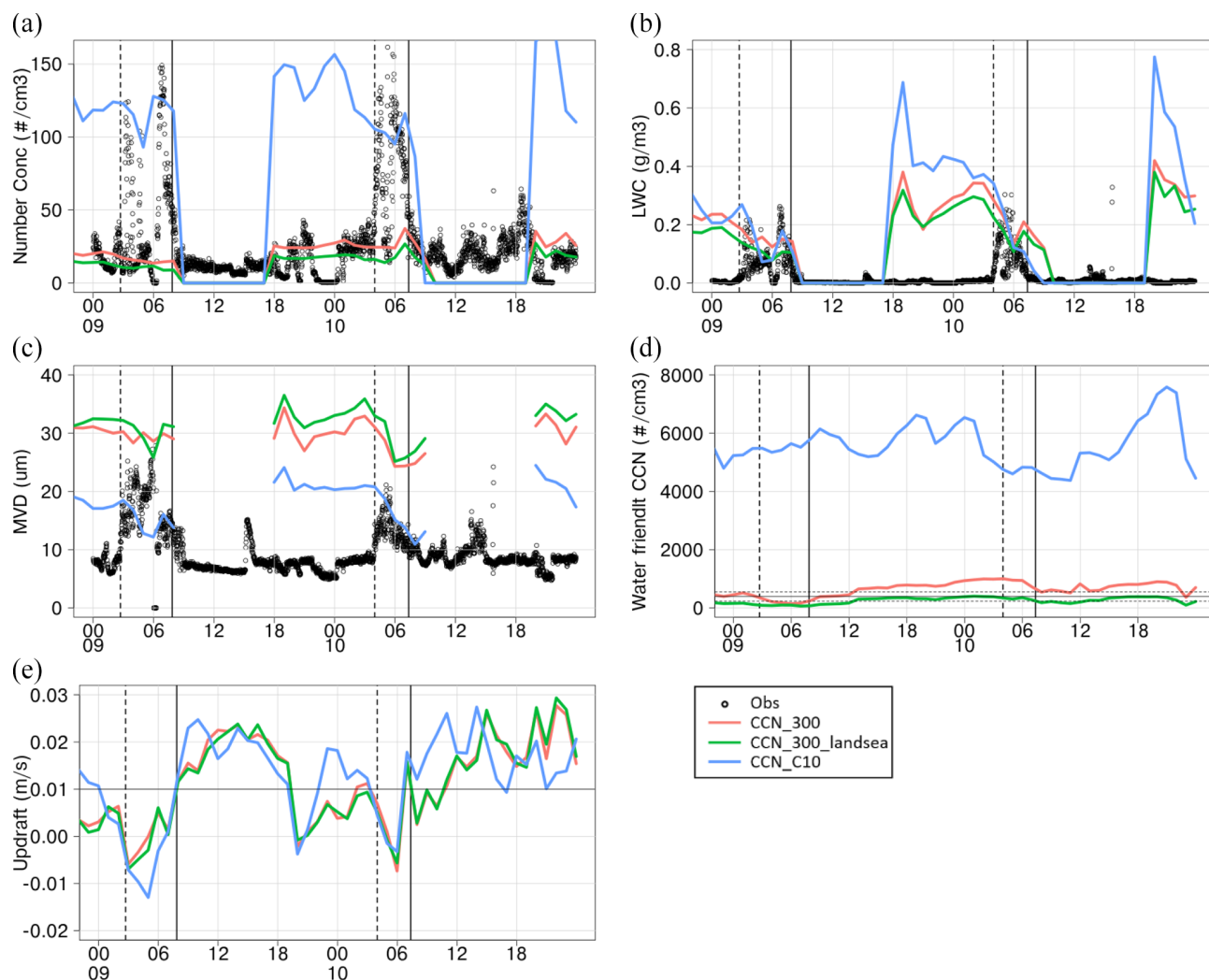
Figure 17. Observed and modelled **(a)** N_t, **(b)** LWC, and **(c)** MVD at Henties Bay. The model is hourly, and black dots are 1 min observations. **(d)** Modelled concentrations of water-friendly aerosols. **(e)** Modelled updraft speed in lowest model level with solid black line at minimum updraft in microphysics scheme. Time is in UTC (site is UTC+2).
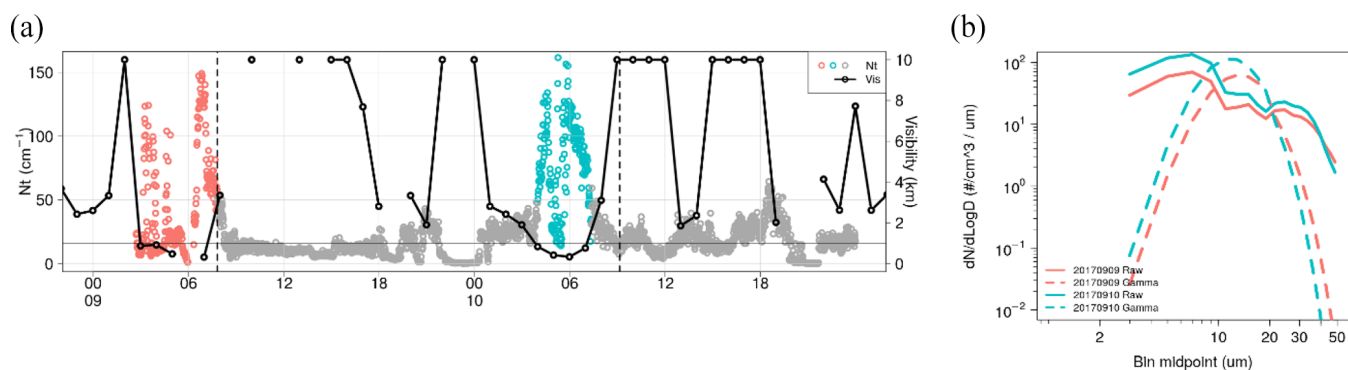
Figure 18. (a) Time series of cloud droplet count (N_t) and visibility. Vertical dashed lines represent sonde release times. The grey horizontal line at 1 km visibility represents fog conditions. Time is in UTC (site is UTC+2). **(b)** Droplet size distribution for the two case studies when visibility was 1 km or less is shown. Colours match with the colours in the time series. Solid lines are the observed distributions. Dashed lines are the equivalent theoretical gamma distribution applied to the observed data.
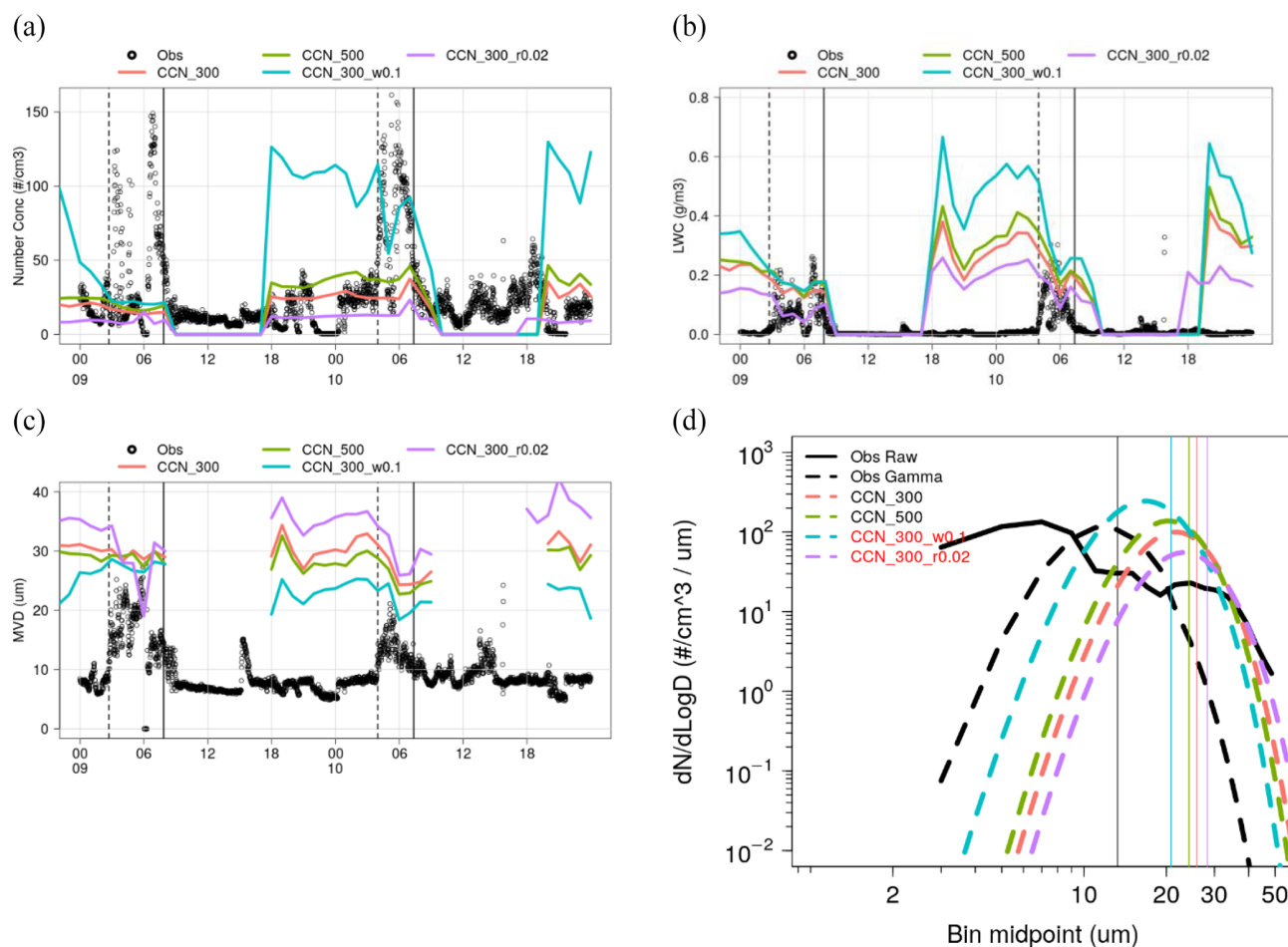
Figure 19. Observed and modelled DSD for **(a)** case 1 and **(b)** case 2. Black solid lines are the observed distributions. Black dashed lines are the equivalent theoretical gamma distribution applied to the observed data. Other dashed lines are model distributions. Vertical solid lines represent the MVD.

surface. Thus, our observed cooling rates are low, which is to be expected. The observed droplet number may then be due to the descent of a mature cloud to the surface, which was initially formed under conditions different to the surface observations. If our fog droplets are indeed from cloud base lowering, then it is possible that our applied updraft speed of $0.1 \, \text{m s}^{-1}$ may be closer to the real conditions at the cloud base. While there are no upper air observations at the site to verify this, it could explain why, when applied at the surface, the cloud droplet number concentrations are in line with the surface observations.

We note that the model does not show this mechanism of CBL. Instead, droplets form in the lowest model level first, and the fog layer thickens over time (as will be shown in Sect. 3.3.4). Thus, the model is missing the initial stratus cloud formation and subsequent cloud base lowering. As indicated in Fig. 7, the model has a cold bias at the surface and, as a result, overestimates relative humidity in the lowest model levels (Fig. 9). This highlights the complexity of the study site which is at the intersection of contrasting land

cover and air mass types (ocean and desert) and that the planetary boundary layer scheme has struggled to simulate this land–sea interface. Adequate modelling of this interface is perhaps an ambitious task and was not the focus of this study from the outset. As a result, the microphysics scheme has activated at a lower altitude that the observations.

As has been discussed, cloud droplets occur every night over the ocean in the simulations, and this cloud deck impinges on the land adjacent to the coastline. To avoid this marine/coastal influence, a second point was extracted from the model about 13 km inland from the study site (labelled inland in Fig. 21). At this point, it is clear that saturation and droplet onset is about 6 h later than the coastal study site (Fig. 21a). The number concentrations are similar between the coastal and inland site, while the LWC is lower than the coastal site. This means that the MVD is also lower, and the DSD shifts to the left, resulting in a closer match the observed DSD (Fig. 21). As before, scenario CCN_300_w0.1 is the best match to the observations in terms of number concentration, LWC, MVD, and DSD.
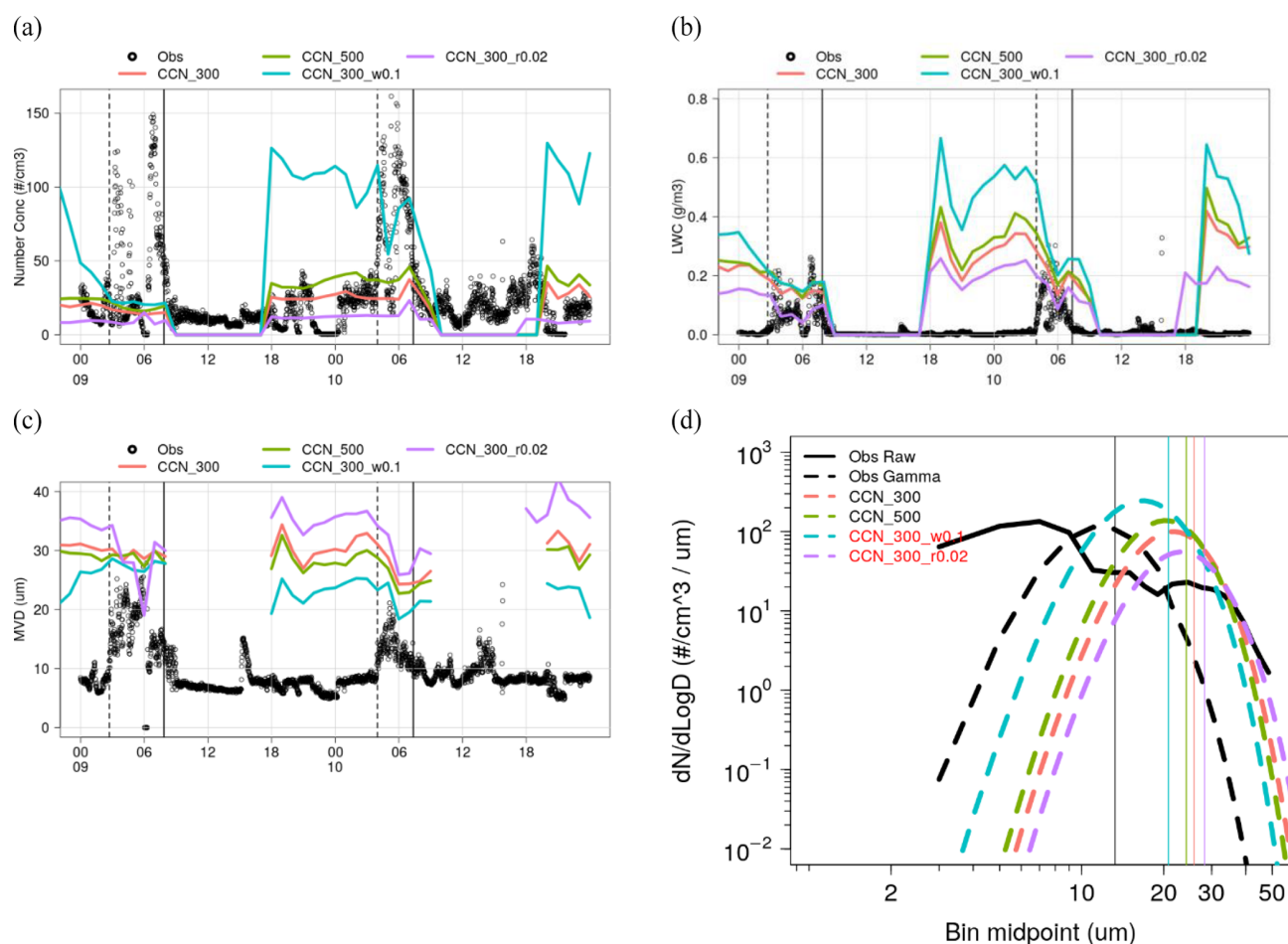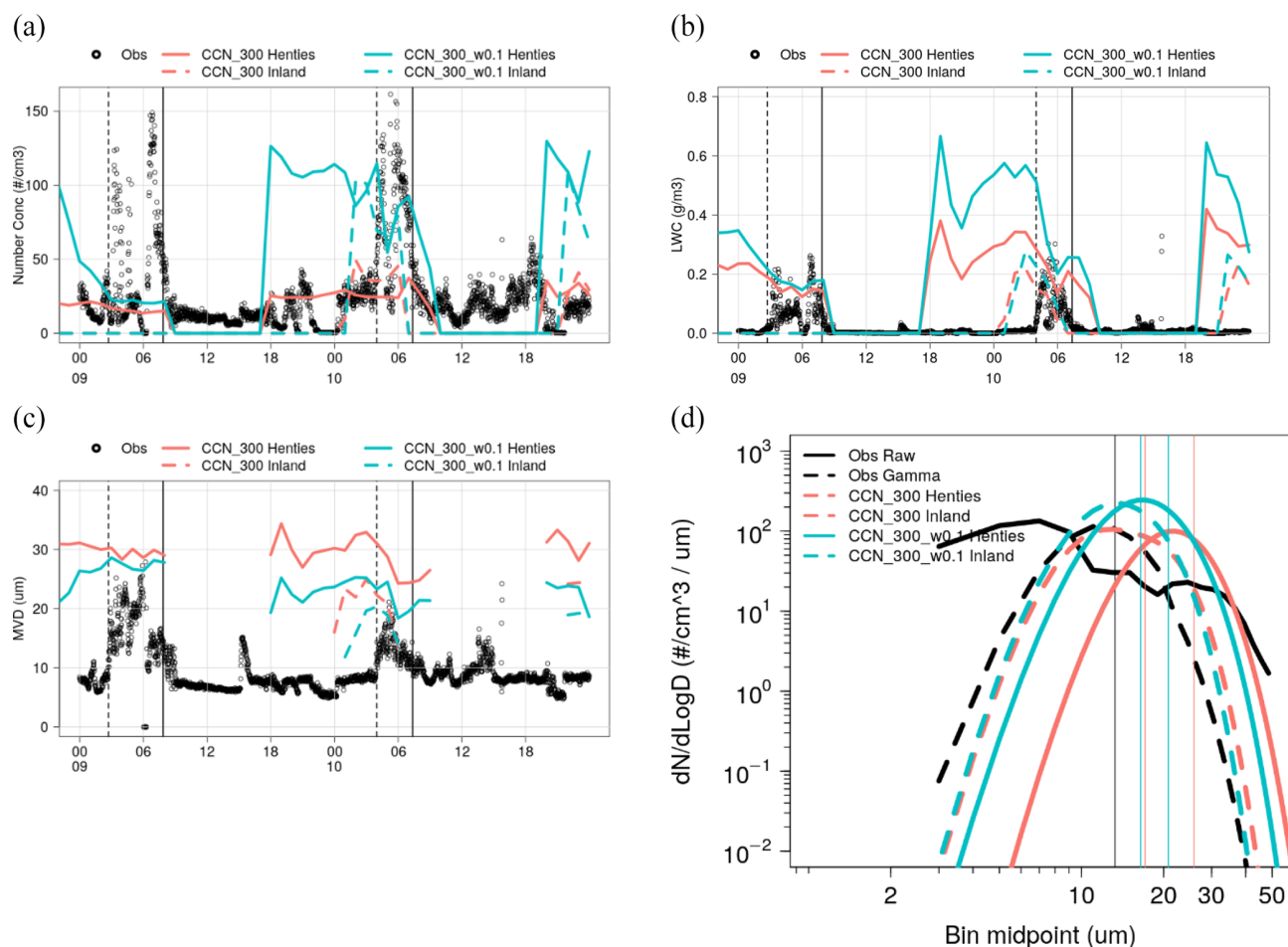
Figure 20. Observed and modelled DSD for **(a)** case 1 and **(b)** case 2. Black solid lines are the observed distributions. Black dashed lines are the equivalent theoretical gamma distribution applied to the observed data. Other dashed lines are model distributions. Vertical solid lines represent the MVD. Time is in UTC (site is UTC+2).

3.3.4 WRF vertical evolution

In this section, we present the fog top height and the vertical evolution of the fog over time (Fig. 22). It was established previously that the fog onset in the model was associated with advection of marine fog. At the time of fog onset, LWC is only present in the lowest model level and incrementally extends to the layers above. Therefore, the model is not exhibiting any cloud base lowering. Cloud base lowering was deduced to have occurred during case 2, where cloud was observed over the site (Fig. 5) hours before visibility decreased to less than 1 km. Fog top was higher for case 2 than case 1. Fog top was about 100 m for case 1 and 220 m for case 2 for the CNN_300 and CNN_300_landsea scenarios, while CNN_C10 showed fog tops at 220 and 300 m, respectively. Spirig et al. (2019) reported fog top at about 350 m a.g.l. at the Gobabeb site, which is about 56 km inland at an elevation of 406 m. Understandably, the model fog top is lower than this, based on the inversion level presented earlier. However, these results demonstrate the benefit of increasing the model

vertical resolution near the ground, as it resolves the fog top height.

4 Conclusions

This study compared WRF model simulations using the Thompson aerosol-aware microphysics scheme to observations for two fog cases that occurred during the AEROCLO-sA field campaign at Henties Bay, Namibia. This scheme was designed with cloud microphysics in mind, more specifically clouds where an updraft is present, but can also simulate fog that occurs under stable conditions and in the lowest model levels. A sensitivity analysis was conducted through variations in the initial CCN concentration, CCN radius, and the minimum updraft speed, which are important factors that influence droplet activation in the microphysics scheme of the model. The first model scenario with initial CCN concentration of $300\,\mathrm{cm}^{-3}$ (CCN_300) underestimated the cloud droplet number concentration, while the LWC was in good

Figure 21. Observed and modelled DSD for **(a)** case 1 and **(b)** case 2. Black solid lines are the observed distributions. Black dashed lines are the equivalent theoretical gamma distribution applied to the observed data. Remaining dashed lines are model distributions. Vertical solid lines represent the MVD. Time is in UTC (site is UTC+2).

agreement with the observations. This resulted in droplet size being larger than the observations. Another scenario used modelled data as CCN initial conditions (CCN_C10) which were an order of magnitude higher than of the first scenario. However, these provided the most realistic values of N_t, LWC, MVD, and DSD. From this it was concluded that CCN activation of about 10 % in the simulations is too low, while the observed appears to be higher, with a mean (median) of 55 % (56 %) during fog events. To achieve this level of activation in the model, the minimum updraft speed for CCN activation was increased from 0.01 to 0.1 m s^{-1} for the scenario CCN_300_w0.1. This scenario provided N_t, LWC, MVD and DSD in the range of the observations, with the added benefit of a realistic initial CCN concentration.

A persistent cloud deck over the ocean was present in the model simulations which impinged on the land immediately adjacent to the ocean. This coincided with the location of the study site and suggests that there is a deficiency in the model physics over water that requires further investigation, as it is

outside the scope of this study. In order to avoid the influence of the persistent impingement, a model grid point was selected about 13 km inland of the study site and compared to the observations. The timing of the case 2 event was more realistic at this point in the model than at the study site. This result, albeit for a case study, is encouraging, as it suggests that if the outstanding issues of the persistent cloud deck and land–sea interface can be addressed, then this model set-up has the ability to produce a realistic timing of events.

The authors acknowledge the limitations of this study due to the low number of cases. However, this is normal for field campaigns over an intensive observation period, and the limited cases have demonstrated the benefits of the aerosol-aware scheme, especially when parameterised with observations. It is hoped that the results are useful to the modelling community and provide some insight to the model sensitivity in simulating fog.
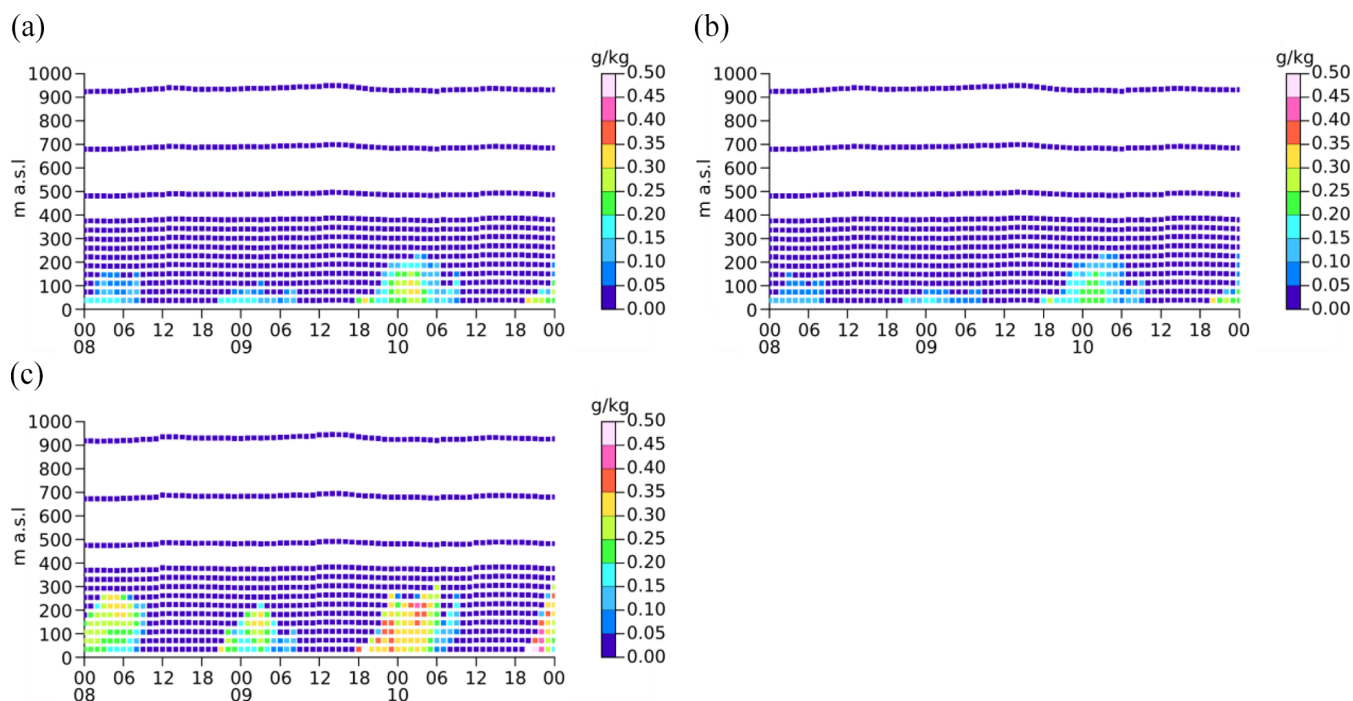
(a)

(b)

(c)

Figure 22. Profiles of LWC over time at Henties Bay for **(a)** CCN_300, **(b)** CCN_300_landsea, and **(c)** CCN_C10. Time is in UTC (site is UTC+2).

Author contributions. MJW conceived the study, designed and performed the analysis, and wrote the original draft. SJP and PF contributed to the data collection and curation, conceptualisation, writing, and reviewing and editing of the original draft. CD, FB, and SB contributed to the data collection and curation and review of original draft. In addition, CD contributed to the methodology of CCN data analysis. TB contributed to the data collection and curation. PF and SJP designed the original AEROCLO-sA observational concept and co-led the 5-year investigation.

Competing interests. At least one of the (co-)authors is a guest member of the editorial board of *Atmospheric Chemistry and Physics* for the special issue "New observations and related modelling studies of the aerosol–cloud–climate system in the Southeast Atlantic and southern Africa regions (ACP/AMT inter-journal SI)". The peer-review process was guided by an independent editor, and the authors also have no other competing interests to declare.

Disclaimer. Publisher's note: Copernicus Publications remains neutral with regard to jurisdictional claims in published maps and institutional affiliations.

Special issue statement. This article is part of the special issue "New observations and related modelling studies of the aerosol–cloud–climate system in the Southeast Atlantic and southern Africa regions (ACP/AMT inter-journal SI)". It is not associated with a conference.

Review statement. This paper was edited by J.M. Haywood and reviewed by two anonymous referees.

References

Ajjaji, R., Al-Katheri, A. A., and Al-Katheri, A. A.: Evaluation of United Arab Emirates WRF two-way nested model on a set of thick coastal fog situations, 8th WRF Users' Workshop. Boulder, Colorado, USA, June 2008, 2008.

Andersen, H. and Cermak, J.: First fully diurnal fog and low cloud satellite detection reveals life cycle in the Namib, Atmos. Meas. Tech., 11, 5461–5470, https://doi.org/10.5194/amt-11-5461-2018, 2018.

Andersen, H., Cermak, J., Solodovnik, I., Lelli, L., and Vogt, R.: Spatiotemporal dynamics of fog and low clouds in the Namib unveiled with ground- and space-based observations, Atmos. Chem. Phys., 19, 4383–4392, https://doi.org/10.5194/acp-19-4383-2019, 2019.

Andersen, H., Cermak, J., Fuchs, J., Knippertz, P., Gaetani, M., Quinting, J., Sippel, S., and Vogt, R.: Synoptic-scale controls of fog and low-cloud variability in the Namib Desert, Atmos. Chem. Phys., 20, 3415–3438, https://doi.org/10.5194/acp-20-3415-2020, 2020.

Bergot, T. and Lestringant, R.: On the predictability of radiation fog formation in a mesoscale model: A case study in heterogeneous terrain, Atmosphere, 10, 1–19, https://doi.org/10.3390/atmos10040165, 2019.

Bott, A.: On the influence of the physico-chemical properties of aerosols on the life cycle of radiation fogs, Bound.-Lay. Meteorol., 56, 1–31, https://doi.org/10.1007/BF00119960, 1991.

Boutle, I., Price, J., Kudzotsa, I., Kokkola, H., and Romakkaniemi, S.: Aerosol-fog interaction and the transition to well-mixed radiation fog, Atmos. Chem. Phys., 18, 7827–7840, https://doi.org/10.5194/acp-18-7827-2018, 2018.

Boutle, I., Angevine, W., Bao, J.-W., Bergot, T., Bhattacharya, R., Bott, A., Ducongé, L., Forbes, R., Goecke, T., Grell, E., Hill, A., Igel, A. L., Kudzotsa, I., Lac, C., Maronga, B., Romakkaniemi, S., Schmidli, J., Schwenkel, J., Steeneveld, G.-J., and Vié, B.: Demistify: a large-eddy simulation (LES) and single-column model (SCM) intercomparison of radiation fog, Atmos. Chem. Phys., 22, 319–333, https://doi.org/10.5194/acp-22-319-2022, 2022.

Branch, O., Schwitalla, T., Temimi, M., Fonseca, R., Nelli, N., Weston, M., Milovac, J., and Wulfmeyer, V.: Seasonal and diurnal performance of daily forecasts with WRF V3.8.1 over the United Arab Emirates, Geosci. Model Dev., 14, 1615–1637, https://doi.org/10.5194/gmd-14-1615-2021, 2021.

Cermak, J.: Low clouds and fog along the South-Western African coast – Satellite-based retrieval and spatial patterns, Atmos. Res.,

116, 15–21, https://doi.org/10.1016/j.atmosres.2011.02.012, 2012.

Che, H. C., Zhang, X. Y., Wang, Y. Q., Zhang, L., Shen, X. J., Zhang, Y. M., Ma, Q. L., Sun, J. Y., Zhang, Y. W., and Wang, T. T.: Characterization and parameterization of aerosol cloud condensation nuclei activation under different pollution conditions, Sci. Rep., 6, 1–14, https://doi.org/10.1038/srep24497, 2016.

Colarco, P., da Silva, A., Chin, M., and Diehl, T.: Online simulations of global aerosol distributions in the NASA GEOS-4 model and comparisons to satellite and ground-based aerosol optical depth, J. Geophys. Res., 115, D14207, https://doi.org/10.1029/2009jd012820, 2010.

Denjean, C. and Bourrianne, T.: AEROCLO-sA PEGASUS CCN concentration, BAOBAB [dataset], https://doi.org/10.6096/AEROCLO.1813, 2021.

Dy, C. Y. and Fung, J. C. H.: Updated global soil map for the Weather Research and Forecasting model and soil moisture initialization for the Noah land surface model, J. Geophys. Res., 121, 8777–8800, https://doi.org/10.1002/2015JD024558, 2016.

Egli, S., Maier, F., Bendix, J., and Thies, B.: Vertical distribution of microphysical properties in radiation fogs – A case study, Atmos. Res., 151, 130–145, https://doi.org/10.1016/j.atmosres.2014.05.027, 2015.

Eidhammer, T., Demott, P. J., and Kreidenweis, S. M.: A comparison of heterogeneous ice nucleation parameterizations using a parcel model framework, J. Geophys. Res.-Atmos., 114, 1–19, https://doi.org/10.1029/2008JD011095, 2009.

EUMETSAT: Best practices for RGB compositing of multi-spectral imagery, User Service Division, 1–8, https://www.eumetsat.int/media/43014 (last access: 5 August 2022), 2009.

Fonseca, R., Francis, D., Weston, M., Nelli, N., Farah, S., Wehbe, Y., AlHosari, T., Teixido, O., and Mohamed, R.: Sensitivity of Summertime Convection to Aerosol Loading and Properties in the United Arab Emirates, Atmosphere, 12, 1687, https://doi.org/10.3390/atmos12121687, 2021.

Formenti, P.: AEROCLO-sA PEGASUS Radiosonde, BAOBAB [data set], https://doi.org/10.6096/AEROCLO.1806, 2020a.

Formenti, P.: AEROCLO-sA PEGASUS Surface Meteorology, BAOBAB [data set], https://doi.org/10.6096/AEROCLO.1808, 2020b.

Formenti, P., D'Anna, B., Flamant, C., Mallet, M., Piketh, S. J., Schepanski, K., Waquet, F., Auriol, F., Brogniez, G., Burnet, F., Chaboureau, J.-P., Chauvigné, A., Chazette, P., Denjean, C., Desboeufs, K., Doussin, J.-F., Elguindi, N., Feuerstein, S., Gaetani, M., Giorio, C., Klopper, D., Mallet, M. D., Nabat, P., Monod, A., Solmon, F., Namwoonde, A., Chikwililwa, C., Mushi, R., Welton, E. J., and Holben, B.: The Aerosols, Radiation and Clouds in Southern Africa Field Campaign in Namibia: Overview, Illustrative Observations, and Way Forward, Bull. Am. Meteorol. Soc., 100, 1277–1298, https://doi.org/10.1175/bams-d-17-0278.1, 2019.

Ghan, S. J., Abdul-Razzak, H., Nenes, A., Ming, Y., Liu, X., Ovchinnikov, M., Shipway, B., Meskhidze, N., Xu, J., and Shi, X.: Droplet nucleation: Physically-based parameterizations and comparative evaluation, J. Adv. Model. Earth Syst., 3, 1–34, https://doi.org/10.1029/2011ms000074, 2011.

Gultepe, I. and Milbrandt, J. A.: Microphysical observations and mesoscale model simulation of warm fog case dur-

ing FRAM project, Pure Appl. Geophys., 164, 1161–1178, https://doi.org/10.1007/s00024-007-0212-9, 2007.

Haeffelin, M., Dupont, J. C., Boyouk, N., Baumgardner, D., Gomes, L., Roberts, G., and Elias, T.: A Comparative Study of Radiation Fog and Quasi-Fog Formation Processes During the ParisFog Field Experiment 2007, Pure Appl. Geophys., 170, 2283–2303, https://doi.org/10.1007/s00024-013-0672-z, 2013.

Haensler, A., Cermak, J., Hagemann, S., and Jacob, D.: Will the southern african west coast fog be affected by future climate change?: Results of an initial fog projection using a regional climate model, Erdkunde, 65, 261–275, https://doi.org/10.3112/erdkunde.2011.03.04, 2011.

Iacono, M. J., Delamere, J. S., Mlawer, E. J., Shephard, M. W., Clough, S. A., and Collins, W. D.: Radiative forcing by long-lived greenhouse gases: Calculations with the AER radiative transfer models, J. Geophys. Res, 113, D13103, https://doi.org/10.1029/2008JD009944, 2008.

Juliano, T. W., Coggon, M. M., Thompson, G., Rahn, D. A., Seinfeld, J. H., Sorooshian, A., and Lebo, Z. J.: Marine boundary layer clouds associated with coastally trapped disturbances: Observations and model simulations, J. Atmos. Sci., 76, 2963–2993, https://doi.org/10.1175/JAS-D-18-0317.1, 2019.

Kain, J. S.: The Kain-Fritsch convective parameterization: an update, J. Appl. Meteorol., 43, 170–181, 2004.

Klopper, D., Formenti, P., Namwoonde, A., Cazaunau, M., Chevaillier, S., Feron, A., Gaimoz, C., Hease, P., Lahmidi, F., Mirande-Bret, C., Triquet, S., Zeng, Z., and Piketh, S. J.: Chemical composition and source apportionment of atmospheric aerosols on the Namibian coast, Atmos. Chem. Phys., 20, 15811–15833, https://doi.org/10.5194/acp-20-15811-2020, 2020.

Lancaster, J., Lancaster, N., and Seely, M. K.: Climate of the central Namib Desert, Madoqua, 1984, 5–61, https://doi.org/10.10520/AJA10115498_484, 1984.

Lee, Z. and Shang, S.: Visibility: How applicable is the century-old Koschmieder model?, J. Atmos. Sci., 73, 4573–4581, https://doi.org/10.1175/JAS-D-16-0102.1, 2016.

Lindesay, J. A. and Tyson, P. D.: Climate and Near-surface Airflow Over the Central Namib, in: Seely, M. K., ed., Namib ecology: 25 years of Namib research, 27–37, Transvaal Museum Monograph No.7, Transvaal Museum, Pretoria, 1990.

Loveland, T. R., Reed, B. C., Ohlen, D. O., Brown, J. F., Zhu, Z., Yang, L., and Merchant, J. W.: Development of a global land cover characteristics database and IGBP DISCover from 1 km AVHRR data, Int. J. Remote Sens., 21, 1303–1330, https://doi.org/10.1080/014311600210191, 2000.

Maalick, Z., Khn, T., Korhonen, H., Kokkola, H., Laaksonen, A., and Romakkaniemi, S.: Effect of aerosol concentration and absorbing aerosol on the radiation fog life cycle, Atmos. Environ., 133, 26–33, https://doi.org/10.1016/j.atmosenv.2016.03.018, 2016.

Maronga, B. and Bosveld, F. C.: Key parameters for the life cycle of nocturnal radiation fog: a comprehensive large-eddy simulation study, Q. J. Roy. Meteorol. Soc., 143, 2463–2480, https://doi.org/10.1002/qj.3100, 2017.

Mazoyer, M., Burnet, F., Denjean, C., Roberts, G. C., Haeffelin, M., Dupont, J. C., and Elias, T.: Experimental study of the aerosol impact on fog microphysics, Atmos. Chem. Phys., 19, 4323–4344, https://doi.org/10.5194/acp-19-4323-2019, 2019.

Muche, G., Kruger, S., Hillmann, T., Josenhans, K., Ribeiro, C., Bazibi, M., Seely, M., Nkonde, E., de Clercq, W., and Strohbach, B.: SASSCAL WeatherNet: present state, challenges, and achievements of the regional climatic observation network and database, Biodiv. Ecol., 6, 34–43, 2018.

Nagel, J.: Fog precipitation measurements on Africa's southwest coast, Notos, 11, 51–60, 1962.

Nakanishi, M. and Niino, H.: An improved Mellor-Yamada Level-3 model: Its numerical stability and application to a regional prediction of advection fog, Bound.-Lay. Meteorol., 119, 397–407, https://doi.org/10.1007/s10546-005-9030-8, 2006.

NCEP: NCEP GFS 0.25 Degree Global Forecast Grids Historical Archive (14) [data set], https://doi.org/10.5065/D65D8PWK, 2015.

Nebuloni, R.: Empirical relationships between extinction coefficient and visibility in fog, Appl. Opt., 44, 3795–3804, https://doi.org/10.1364/AO.44.003795, 2005.

Olivier, J.: Spatial distribution of fog in the Namib, J. Arid Environ., 29, 129–138, https://doi.org/10.1016/S0140-1963(05)80084-9, 1995.

Poku, C., Ross, A. N., Blyth, A. M., Hill, A. A., and Price, J. D.: How important are aerosol–fog interactions for the successful modelling of nocturnal radiation fog?, Weather, 74, 237–243, https://doi.org/10.1002/wea.3503, 2019.

Poku, C., Ross, A. N., Hill, A. A., Blyth, A. M., and Shipway, B.: Is a more physical representation of aerosol activation needed for simulations of fog?, Atmos. Chem. Phys., 21, 7271–7292, https://doi.org/10.5194/acp-21-7271-2021, 2021.

Price, J.: Radiation Fog, Part I: Observations of Stability and Drop Size Distributions, Bound.-Lay. Meteorol., 139, 167–191, doi10.1007/s10546-010-9580-2, 2011.

Román-Cascón, C., Steeneveld, G. J., Yagüe, C., Sastre, M., Arrillaga, J. A., and Maqueda, G.: Forecasting radiation fog at climatologically contrasting sites: evaluation of statistical methods and WRF, Q. J. Roy. Meteorol. Soc., 142, 1048–1063, https://doi.org/10.1002/qj.2708, 2016.

Román-Cascón, C., Yagüe, C., Steeneveld, G.-J., Morales, G., Arrillaga, J. A., Sastre, M., and Maqueda, G.: Radiation and cloud-base lowering fog events: Observational analysis and evaluation of WRF and HARMONIE, Atmos. Res., 229, 190–207, https://doi.org/10.1016/j.atmosres.2019.06.018, 2019.

Saleeby, S. M. and Cotton, W. R.: A large-droplet mode and prognostic number concentration of cloud droplets in the Colorado State University Regional Atmospheric Modeling System (RAMS), Part I: Module descriptions and supercell test simulations, J. Appl. Meteorol., 43, 182–195, https://doi.org/10.1175/1520-0450(2004)043<0182:ALMAPN>2.0.CO;2, 2004.

Sanchez, P. A., Ahamed, S., Carre, F., Hartemink, A. E., Hempel, J., Huising, J., Lagacherie, P., McBratney, A. B., McKenzie, N. J., Mendonça-Santos, M. d. L., Minasny, B., Montanarella, L., Okoth, P., Palm, C. A., Sachs, J. D., Shepherd, K. D., Vågen, T.-G., Vanlauwe, B., Walsh, M. G., Winowiecki, L. A., and Zhang, G.-L.: Digital soil map of the world, Science, 325, 680–681, https://doi.org/10.1126/science.1175084, 2009.

Schmetz, J., Pili, P., Tjemkes, S., Just, D., Kerkmann, J., Rota, S., and Ratier, A.: An introduction to Meteosat Second Generation (MSG), Bull. Am. Meteo-

rol. Soc., 83, 977–992, https://doi.org/10.1175/1520-0477(2002)083<0977:AITMSG>2.3.CO;2, 2002.

Seely, M. and Henschel, J. R.: The climatology of Namib fog, Conference on Fog and Fog Collection, Vancouver, Canada, 19–24, 1998.

Seely, M. K. and Hamilton, W. J.: Fog catchment sand trenches constructed by tenebrionid beetles, Lepidochora, from the Namib Desert, Science, 193, 484–486, https://doi.org/10.1126/science.193.4252.484, 1976.

Seinfeld, J. H. and Pandis, S. N.: Atmospheric chemistry and physics: from air pollution to climate change, John Wiley & Sons, Seinfeld and Pandis, ISBN 978-1-118-94740-1, 2016.

Sertel, E., Robock, A., and Ormeci, C.: Impacts of land cover data quality on regional climate simulations, Int. J. Climatol., 30, 1942–1953, https://doi.org/10.1002/joc.2036, 2010.

Skamarock, W. C., Klemp, J. B., Dudhia, J., Gill, D. O., Barker, D. M., Duda, M. G., Huang, X.-Y., Wang, W., and Powers, J. G.: A Description of the Advanced Research WRF Version 3, NCAR, Tech. Rep., NCAR/TN–475+STRg, https://doi.org/10.5065/D68S4MVH, 2008.

Spiegel, J. K., Zieger, P., Bukowiecki, N., Hammer, E., Weingartner, E., and Eugster, W.: Evaluating the capabilities and uncertainties of droplet measurements for the fog droplet spectrometer (FM-100), Atmos. Meas. Tech., 5, 2237–2260, https://doi.org/10.5194/amt-5-2237-2012, 2012.

Spirig, R., Vogt, R., Larsen, J. A., Feigenwinter, C., Wicki, A., Franceschi, J., Parlow, E., Adler, B., Kalthoff, N., Cermak, J., Andersen, H., Fuchs, J., Bott, A., Hacker, M., Wagner, N., Maggs-Klling, G., Wassenaar, T., and Seely, M.: Probing the fog life cycles in the Namib desert, Bull. Am. Meteorol. Soc., 100, 2491–2507, https://doi.org/10.1175/BAMS-D-18-0142.1, 2019.

Statista: Namibia: Population density from 2008 to 2018, https://www.statista.com/statistics/971467/population-density-in-namibia/ (last access: 5 August 2022), 2020.

Steeneveld, G. J. and de Bode, M.: Unravelling the relative roles of physical processes in modelling the life cycle of a warm radiation fog, Q. J. Roy. Meteorol. Soc., 144, 1539–1554, https://doi.org/10.1002/qj.3300, 2018.

Stolaki, S., Haeffelin, M., Lac, C., Dupont, J. C., Elias, T., and Masson, V.: Influence of aerosols on the life cycle of a radiation fog event. A numerical and observational study, Atmos. Res., 151, 146–161, https://doi.org/10.1016/j.atmosres.2014.04.013, 2015.

Tardif, R.: The impact of vertical resolution in the explicit numerical forecasting of radiation fog: A case study, Pure Appl. Geophys., 164, 1221–1240, https://doi.org/10.1007/s00024-007-0216-5, 2007.

Thompson, G. and Eidhammer, T.: A Study of Aerosol Impacts on Clouds and Precipitation Development in a Large Winter Cyclone, J. Atmos. Sci., 71, 3636–3658, https://doi.org/10.1175/JAS-D-13-0305.1, 2014.

Weston, M., Temimi, M., Morais, R., Reddy, N., Francis, D., and Piketh, S.: A rule-based method for diagnosing radiation fog in an arid region from NWP forecasts, J. Hydrol., 597, 126189, https://doi.org/10.1016/j.jhydrol.2021.126189, 2021.

Weston, M. J. and Temimi, M.: Application of a night time fog detection method using SEVIRI over an arid environment, Remote Sens., 12, 2281, https://doi.org/10.3390/rs12142281, 2020.

Wilkinson, J. M., Porson, A. N. F., Bornemann, F. J., Weeks, M., Field, P. R., and Lock, A. P.: Improved microphysical parametrization of drizzle and fog for operational forecasting using the Met Office Unified Model, Q. J. Roy. Meteorol. Soc., 139, 488–500, https://doi.org/10.1002/qj.1975, 2013.

World Meteorological Organization: Aerodrome reports and forecasts: a users' handbook to the codes, WMO, ISBN 978-92-63-10782-4, 81, 2008.

WRF Users Page: Notes for running WRF with the Aerosol-aware Thompson Scheme (mp_physics = 28), https://www2.mmm.ucar.edu/wrf/users/physics/mp28_updated.html (last access: 5 August 2022), 2020.

Zeng, X. and Beljaars, A.: A prognostic scheme of sea surface skin temperature for modeling and data assimilation, Geophys. Res. Lett., 32, 1–4, https://doi.org/10.1029/2005GL023030, 2005.

Zhou, B., Du, J., Gultepe, I., and Dimego, G.: Forecast of low visibility and fog from NCEP: Current status and efforts, Pure Appl. Geophys., 169, 895–909, https://doi.org/10.1007/s00024-011-0327-x, 2012.